Research Square

Preprints are preliminary reports that have not undergone peer review.
They should not be considered conclusive, used to inform clinical practice,
or referenced by the media as validated information.

Molecular Insights into Catalysis and Inhibition of Human Phosphatidylethanolamine Methylation

Dianfan Li

dianfan.li@sibcb.ac.cn

School of Agriculture and Biotechnology, Sun Yat-sen University https://orcid.org/0000-0003-4729-4678

Tingting Li

School of Agriculture and Biotechnology, Sun Yat-sen University

Hao Xia

State Key Laboratory of Molecular Biology, Shanghai Institute of Biochemistry and Cell Biology, Center for Excellence in Molecule Cell Science, Chinese Academy of Sciences

Yulin Chao

Shanghai Stomatological Hospital, School of Stomatology, Shanghai Key Laboratory of Medical Epigenetics, International Co-laboratory of Medical Epigenetics and Metabolism, Fudan University

Jiaxiao Lin

School of Agriculture and Biotechnology, Sun Yat-sen University

Zhihao Yue

School of Agriculture and Biotechnology, Sun Yat-sen University

Qianhui Qu

Fudan University https://orcid.org/0000-0002-5753-2599

Biological Sciences - Article

Keywords:

Posted Date: September 2nd, 2026

DOI: https://doi.org/10.21203/rs.3.rs-10717599/v1

License: This work is licensed under a Creative Commons Attribution 4.0 International License.
Read Full License

Additional Declarations: There is **NO** Competing Interest.

Title:

Molecular Insights into Catalysis and Inhibition of Human Phosphatidylethanolamine Methylation

Authors:

Tingting Li[1,†], Hao Xia[2,†], Yulin Chao[3,†], Jiaxiao Lin[1], Zhihao Yue[1], Qianhui Qu[3,*], Dianfan Li[1,*]

Affiliations:

[1]School of Agriculture and Biotechnology, Sun Yat-sen University, Shenzhen, 518107, China.

[2]Center for Excellence in Molecular Cell Science, Shanghai Institute of Biochemistry and Cell Biology, University of CAS, Chinese Academy of Sciences (CAS), 320 Yueyang Road, Shanghai 200031, China.

[3]Eye & ENT Hospital, Institutes of Biomedical Sciences, Shanghai Key Laboratory of Medical Epigenetics, International Co-laboratory of Medical Epigenetics and Metabolism (Ministry of Science and Technology), Department of Systems Biology for Medicine, Fudan University, Shanghai 200032, China.

[†]Equal contribution. [*]Correspondence: qqh@fudan.edu.cn, lidf9@mail.sysu.edu.cn

ABSTRACT

Phospholipid homeostasis is essential for membrane function, lipid metabolism, and liver physiology. The integral membrane enzyme PEMT maintains the phosphatidylcholine/phosphatidylethanolamine (PC/PE) balance by sequentially methylating PE using *S*-adenosylmethionine (SAM). PEMT deficiency protects mice against diet-induced obesity and atherosclerosis, while the clinical antihypertensive drug clofibric acid (CFA) inhibits PEMT and produces related effects on lipid and lipoprotein metabolism. However, the molecular basis of PEMT function has remained unknown. Here, we report five cryo-EM structures of human PEMT in PE/*S*-adenosylhomocysteine (SAH)-, PE/SAM-, PC/SAH-, CFA-bound, and cofactor-free states at 3.26–2.53 Å resolution. The structures reveal the molecular basis of substrate recognition, support an ordered Bi-Bi catalytic mechanism with a largely preorganized active site, identify a gating mechanism for cofactor exchange, and show how CFA occupies the PE-binding site to inhibit PEMT. These findings establish the structural basis of PEMT function and provide a framework for future structure-guided development of selective PEMT modulators.

INTRODUCTION

The balance between phosphatidylcholine (PC) and phosphatidylethanolamine (PE), the two most abundant membrane lipids in mammalian cells, is a central determinant of membrane biophysics, lipid and lipoprotein metabolism, and cellular energy homeostasis (summarized in refs. [1,2]). In the liver, this balance is regulated by phosphatidylethanolamine *N*-methyltransferase (PEMT), a small (~20 kDa) endoplasmic reticulum (ER) membrane enzyme that catalyzes three sequential methylation reactions converting PE to PC using *S*-adenosylmethionine (SAM) as the methyl donor (**Fig. S1a**). PEMT accounts for 30% of hepatic PC production and provides the sole *de novo* source of choline[3,4]. By linking one-carbon metabolism to phospholipid biosynthesis, PEMT influences membrane composition, lipid and lipoprotein metabolism, mitochondrial function, cellular energy homeostasis, and the cellular methylation landscape[1,2,5-7]. Human PEMT polymorphisms have been associated with metabolic disorders[8], cardiovascular disease[9], cancers[10-13], developmental abnormalities[14,15], and non-alcoholic steatohepatitis (NASH) [16-22]. PEMT preferentially generates polyunsaturated PC species, including docosahexaenoic acid (DHA)-containing PC[23-26], linking its activity to neuronal function and development. Thus, reduced PEMT activity has been associated with Alzheimer's disease[27], whereas PEMT genetic variations influences DHA levels in children[28] and PEMT-derived choline and DHA contribute to fetal development[24,29,30].

Genetic ablation of PEMT produces one of the most striking metabolic phenotypes observed for a phospholipid biosynthetic enzyme. PEMT-knockout mice[31] are protected from diet-induced obesity and insulin resistance[32], exhibit markedly reduced atherosclerosis[33], and are resistant to diabetic kidney injury[34]. These beneficial phenotypes arise from coordinated metabolic rewiring, including impaired hepatic very-low-density lipoprotein (VLDL) secretion[35], improved insulin signalling[36], increased thermogenesis[37], reduced gluconeogenesis[38], enhanced mitochondrial respiration[38], increased coenzyme Q synthesis[39], and reduced homocysteine

production[40,41]. In peripheral tissues, PEMT deficiency further suppresses adipogenesis[42], lipogenesis[37], and lipid droplet formation[43], while altering calcium handling in skeletal muscle[44], collectively increasing whole-body energy expenditure.

Despite these promising metabolic phenotypes, complete loss of PEMT is detrimental. PEMT-knockout mice develop steatosis, cholestasis[45], and even liver failure[46] under choline-deficient conditions while liver regeneration following injury is impaired[45-47]. Reduced PEMT expression is likewise observed in hepatocarcinogenesis models[48-50] and in patients with alcoholic cirrhosis[51] and hepatocellular carcinoma[52], where expression correlates with disease progression and survival. These findings instead point to controlled pharmacological modulation of PEMT as a more promising therapeutic strategy. Recent studies support this concept by showing that antihypertensive[53], antidiabetic[54], and antioxidant treatments[55] alleviate the hepatic stress associated with PEMT deficiency while preserving protection against obesity and insulin resistance, suggesting that the adverse consequences of reduced PEMT activity may be manageable. These observations provide a strong rationale for developing pharmacological modulators of PEMT.

Clofibric acid (CFA), a clinically used antihypertensive drug that also activates peroxisome proliferator-activated receptor alpha (PPARα), provides an intriguing pharmacological link to PEMT. CFA has long been known to inhibit PE methylation[56,57], and studies in rat hepatocytes showed that CFA treatment alters PC molecular species[58], reduces VLDL secretion and alters hepatic triacylglycerol and lipoprotein metabolism[59], recapitulating selected aspects of the metabolic phenotypes associated with PEMT deficiency[31,33]. However, the molecular basis of CFA inhibition of PEMT has remained unknown. Defining this interaction is therefore important for understanding PEMT pharmacology and for guiding the development of selective PEMT modulators.

Here, we report five cryo-EM structures of human PEMT determined in lipid nanodiscs and detergent micelles, capturing distinct catalytic and inhibitory states in complex with

PE, PC, SAM, *S*-adenosylhomocysteine (SAH), and CFA at resolutions of 3.26–2.53 Å. Together, these structures reveal how a remarkably compact membrane enzyme coordinates a membrane-embedded lipid substrate with a soluble methyl donor, define the molecular basis of substrate recognition, catalysis, and CFA inhibition, and uncover a helix-mediated gating mechanism for cofactor exchange that provides a structural rationale for the reduced activity associated with the V175M variant. These findings establish a framework for understanding PEMT regulation and for future structure-guided development of selective PEMT modulators.

RESULTS

Biochemical characterization of human PEMT in micelles and lipid nanodiscs

Human PEMT (hPEMT) exists as two isoforms: a shorter, catalytically more active form (~20 kDa) and a longer isoform (~26 kDa) containing a glycosylated N-terminal extension[60]. The construct used in this study corresponds to the short isoform and carries the naturally occurring Met175[16,18,19,27] and Ile58[61] variants. Hereafter referred to as wild-type (WT) hPEMT, it was recombinantly expressed in HEK293 cells with a C-terminal thermostable GFP (TGP) tag. Purified TGP-tagged hPEMT retained robust transmethylation activity, as measured using ^{3}H-labeled SAM in Triton X-100 (**Fig. S1b**). Kinetic analysis with varying SAM concentrations followed Michaelis-Menten behavior, reporting a K_m(SAM) of 1.8 μM and a V_{max} of 13.5 nmol·min^{-1}·mg^{-1} (**Fig. 1a**). In contrast, activity increased non-saturably with PE concentration (**Fig. S1c**), consistent with previous observations for rat PEMT and its dependence on a membrane-like lipid environment[4]. To better mimic the native membrane, hPEMT was reconstituted into lipid nanodiscs containing phospholipids, including PE. The reconstituted enzyme remained catalytically active (**Fig. S1b**), establishing a functional bilayer system suitable for structural analysis.

Neutral and inhibitory synthetic nanobodies against hPEMT

Because hPEMT (22.8 kDa) is too small for single-particle cryo-EM, we adopted a legobody strategy[62] in which a target-specific synthetic nanobody (sybody) recruits a ~120-kDa fiducial module to facilitate particle alignment. Screening sybody libraries[63] against hPEMT reconstituted in lipid nanodiscs identified LB11, which did not affect enzymatic activity (**Fig. S1d**). Screening hPEMT in lauryl maltose neopentyl glycol (LMNG) detergent micelles yielded a second sybody, SC3. In contrast to LB11, SC3 inhibited hPEMT (IC50 = 83 nM), but only in lauryl maltose neopentyl glycol (LMNG) and not in Triton X-100 (**Fig. S1e**).

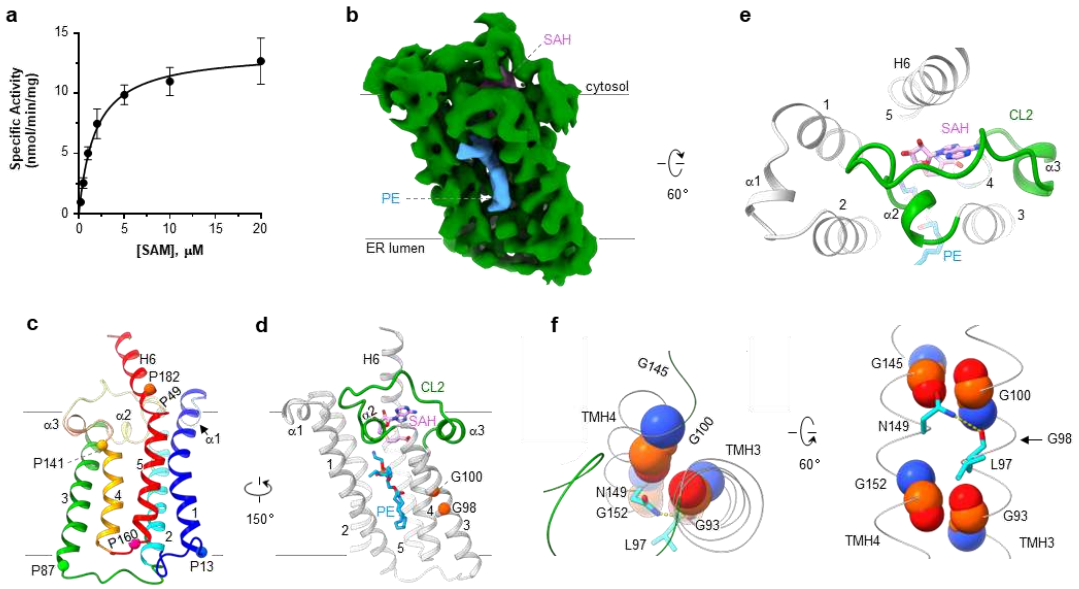


Fig. 1 | Structure and functional characterization of human PEMT. a Activity of hPEMT as a function of SAM concentration. Data represent mean ± s.d. from three independent experiments. **b** Cryo-EM map of hPEMT (green) with densities for PE (cyan) and SAH (magenta). Densities corresponding to the sybody and legobody are omitted for clarity. **c-e** Structure of hPEMT viewed from the membrane plane (**c, d**) and in a titled orientation (**e**). Structural elements discussed in the text are labelled. **f** Glycine zipper-mediated packing between transmembrane helix (TMH) 3 and 4.

Overall architecture and active site organization

We first determined the cryo-EM structure of hPEMT reconstituted in lipid nanodiscs using LB11-based legobody. The resulting structure was resolved to 2.53-Å resolution (**Fig. 1b, Fig. S2, Table S1**). Consistent with its lack of effect on enzymatic activity, LB11 binds the limited luminally exposed surface of hPEMT (**Fig. S3a**), distal to the cytosolic active site. The high-quality density enabled near-complete model building, with only eight C-terminal residues unresolved. Consistent with previous biochemical observations[60], no glycosylation was detected in the cryo-EM map. The structure also resolved two ligands, a PE molecule presumably derived from the nanodisc and a SAH molecule retained during purification (designated hPEMT^{PE+SAH}), thereby defining the active site (**Fig. 1b**).

hPEMT adopts a compact architecture comprising five transmembrane helices (TMHs), with its N terminus in the ER lumen and its C terminus in the cytosol (**Fig. 1c**). With the exception of cytosolic loop 2 (CL2) and a short C-terminal helix (H6), the protein is almost entirely embedded within the membrane. Notably, each TMH is preceded by a conserved proline residue (**Fig. 1c, Fig. S4**), a feature that may contribute to helix packing and membrane topology.

A central challenge for PEMT is to bring together a water-soluble cofactor and a membrane-embedded lipid substrate within a small monomeric protein. The structure reveals that this is achieved through a highly compact architecture organized around the active site. The five transmembrane helices (TMHs) pack tightly on the luminal side, whereas TMH5 tilts away from the helical bundle and the cytosolic half of TMH1 bends outward, creating a lateral opening bounded by TMH1/2, TMH3/4, and TMH5 that provides membrane access for the lipid substrate (**Fig. 1d, 1e**). On the cytosolic side, the active site is enclosed by CL2 and the short C-terminal helix H6. H6 bends sharply towards CL2 at the conserved Pro182, sealing the cofactor-binding pocket from the cytosol while leaving the lipid-entry pathway accessible from the membrane (**Fig. 1d, 1e**).

CL2 plays a central architectural role. This unusually long loop (27 residues) contains two amphipathic helices (α2 and α3) that interact extensively with the membrane while simultaneously contacting multiple TMHs, thereby creating a stable, partially membrane-buried pocket for SAM binding. This architecture is stabilized by close packing between TMH3 and TMH4, mediated by a glycine zipper motif characteristic of membrane proteins[64,65]. An additional intramembrane hydrogen bond between Asn149 and the backbone carbonyl of Leu97 further reinforces this interface (**Fig. 1f**). Consistent with its structural importance, mutation of Gly100 abolishes activity, whereas G98A reduces SAM binding and methyltransferase activity[66] despite both residues being distant from the cofactor-binding site (**Fig. 1d**).

PE recognition balances specificity and flexibility

PE binds within a membrane-buried cavity involving all TMHs (**Fig. 1e**). The ethanolamine headgroup is enclosed by a conserved aromatic cage formed by Trp29, Phe117, and Tyr143, together with Ile60 and Met142, while the glycerophosphate group is anchored by Arg67 and additional polar interactions involving Asn64 and Tyr173 (**Fig. 2a**). Consistent with the importance of this recognition network, alanine substitution of the aromatic-cage residues, Met142, or Arg67 drastically reduced or abolished enzymatic activity (**Fig. 2b**). By contrast, mutations of residues making peripheral polar contacts, such as S146A and Y173F, retained substantial activity, suggesting that these interactions contribute to substrate stabilization rather than defining the recognition site.

This stringent headgroup recognition contrasts with the permissive accommodation of the acyl chains. The two acyl chains extend into a relatively spacious hydrophobic chamber with limited specific contacts (**Fig. 2a**). One chain extends toward the luminal side, whereas the other remains near the membrane interface. Thus, PEMT appears to use a two-tiered recognition strategy, with stringent recognition of the conserved phosphoethanolamine headgroup coupled to permissive accommodation of structurally diverse acyl chains. This architecture enables PEMT to accommodate PE species with diverse acyl-chain compositions[23-26] while maintaining a productive geometry for sequential headgroup methylation.

A precisely organized cofactor pocket

SAH occupies a compact pocket formed predominantly by CL2, where its adenosine and homocysteine moieties are tightly coordinated within the small membrane-embedded active site (**Fig. 2c**). The adenine base is clamped between Phe135/Leu111 and Thr184, while Arg129, positioned by Asp139 at the tip of TM3, hydrogen bonds with the exocyclic amine of adenine. Consistent with the importance of this interaction network, F135L caused an ~95% loss of activity, whereas R129Q and R129A reduced activity by ~50% and ~67%, respectively. The ribose is coordinated by the conserved

Asp120, whose substitution with alanine also markedly impaired activity (**Fig. 2d**). At the homocysteine end, SAH packs against Met142 and Tyr143, residues that also contribute to PE recognition (**Fig. 2a**). The position of Tyr143 is further stabilized by Glu180, explaining why E180A abolishes activity[66] despite Glu180 not directly contacting SAH (**Fig. 2c, 2d**). The SAH carboxylate additionally forms hydrogen bonds with backbone amides near Pro141 and neutralizes the otherwise unsatisfied positive dipole at the end of TMH4, thereby stabilizing the bent conformation of the cofactor. Together, these interactions precisely position SAH within the compact active site while coupling cofactor recognition to the structural elements that also participate in lipid-substrate binding.

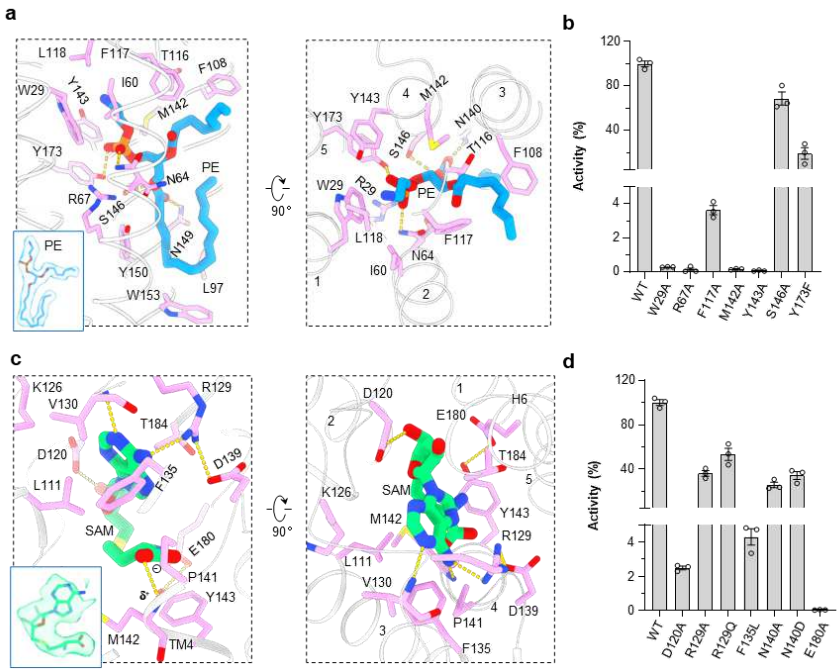


Fig. 2 | Molecular basis of PE and SAH recognition. a Interactions between PE (blue) and hPEMT (white cartoon), with interacting residues shown as pink sticks. Dashed lines indicate distances within 3.4 Å. The corresponding cryo-EM density is shown in the inset. **b** Activities of hPEMT mutants targeting the PE-binding pocket. **c** Interactions between SAH (green) and hPEMT (pink), with the corresponding cryo-EM density shown in the inset. **d** Activities of hPEMT mutants targeting the SAM-binding pocket. Numbers indicate transmembrane helices (TMHs). Data in **b** and **d** represent mean ± s.e.m. from three independent experiments.

A ternary complex positions PE and SAM for methyl transfer

To capture a catalytically relevant ternary complex, we exploited the inhibitory sybody SC3 and assembled the SC3-legobody complex in LMNG micelles in the presence of PE and SAM. The resulting structure, determined at 3.26-Å resolution (**Fig. 3a, Fig. S5, Table S1**) and designated hPEMT^{PE+SAM}, closely resembles the hPEMT^{PE+SAH} structure, with an all-atom root-mean-square deviation (RMSD) of 0.80 Å. Unlike LB11, SC3 binds the cytosolic surface of hPEMT. Its complementarity-determining region 3 (CDR3) inserts into a groove between H6 and TMH1, whereas CDR1 and the framework region establish additional contacts with the limited cytosolic surface (**Fig. S6a, S6b**). Consistent with its detergent-dependent inhibition, the maltose headgroup of LMNG bridges SC3 and hPEMT through an extensive interaction network involving eight hydrogen bonds (**Fig. S6c**).

The cryo-EM density unambiguously resolves a complete SAM molecule together with the PE headgroup and proximal portions of the lipid (**Fig. 3a**), capturing a catalytically poised ternary complex. Within the active site, the PE amine and the transferable methyl group of SAM are positioned along a common reaction trajectory, with the methyl carbon oriented for nucleophilic attack by the PE amine (**Fig. 3b**). This geometry supports an in-line methyl-transfer mechanism in which the PE amine attacks the electrophilic methyl carbon from the side opposite the sulfonium sulfur, concomitant with cleavage of the S–C bond. The positive charge of the sulfonium center facilitates methyl transfer by polarizing the S–C bond and is neutralized upon departure of SAH. Repetition of this reaction three times ultimately converts PE into PC.

To define the product-bound state, we also determined a structure simultaneously containing PC and SAH using SC3 (hPEMT^{PC+SAH}, 3.00-Å resolution; **Fig. 3c, Fig. S7, Table S1**). Comparison of hPEMT^{PE+SAM} and hPEMT^{PC+SAH} reveals remarkably little structural variation, even at the level of active-site side chains (**Fig. 3d**). Together with the simultaneous visualization of both substrates, these observations indicate that PEMT employs a largely pre-organized active site in which precise alignment of the reacting groups facilitates catalysis.

Movement of the C-terminal helix (H6) gates SAM/SAH exchange

In contrast to the laterally accessible PE-binding cavity, the SAM/SAH-binding pocket is deeply buried within the protein, suggesting that cofactor exchange requires a transient opening of the active site. To capture this state, we determined the structure of the cofactor-binding mutant D120A at 2.74 Å resolution (**Fig. S8, Table S1**). The overall structure (designated $hPEMT^{PE}$) remains highly similar to the cofactor-bound $hPEMT^{PE+SAH}$ (Cα RMSD of 0.41 Å), indicating that SAM/SAH exchange does not require global rearrangement. Instead, the structural differences are concentrated in the local elements that define the cofactor-binding pocket, namely CL2 and H6. In the absence of SAH, CL2 undergoes modest rearrangement (**Fig. 3e**).

The most prominent transition occurs in the C-terminal helix (H6), which undergoes a pronounced ~20° rotation away from the cofactor-binding pocket, pivoting around Leu177 (**Fig. 3e, 3f**). This movement shifts the tip of H6 by approximately 6 Å and disrupts interactions that stabilize the closed conformation, including the Arg129-Asp139 salt bridge and the Asn140-Glu181 hydrogen bond (**Fig. 3f**). Consequently, a solvent-accessible pathway is created for SAM/SAH exchange (**Fig. 3g, Movie 1**), whereas this route is occluded in the ligand-bound state (**Fig. 3h**). These observations identify H6 as a molecular gate that controls access to the buried cofactor-binding pocket. Consistent with this model, the open conformation is incompatible with SC3 binding because outward movement of H6 repositions Ile187 and other residues that would clash with the CDR3 loop of SC3 (**Fig. 3i–3k**). Thus, SC3 binding stabilizes the closed conformation, providing further structural support for H6-mediated control of SAM/SAH exchange.

This gating mechanism also provides a potential explanation for the disease-associated V175M polymorphism[16,18,19,27]. Residue 175 lies adjacent to the hinge region that enables H6 rotation (**Fig. 3f**). Valine, with its β-branched side chain, may increase local helix flexibility, facilitating H6 movement and efficient cofactor exchange. In contrast, methionine has a substantially greater helix-forming propensity[67] and is therefore

expected to stabilize the TMH5-H6 segment and restrict its mobility. Such stabilization would reduce opening of the cofactor-binding pocket and slow SAM/SAH exchange, consistent with the lower activity of the Met175 variant reported previously[19] and confirmed in this study (**Fig. S1f**). The effect of the V175M substitution on local helix dynamics, however, remains to be directly established.

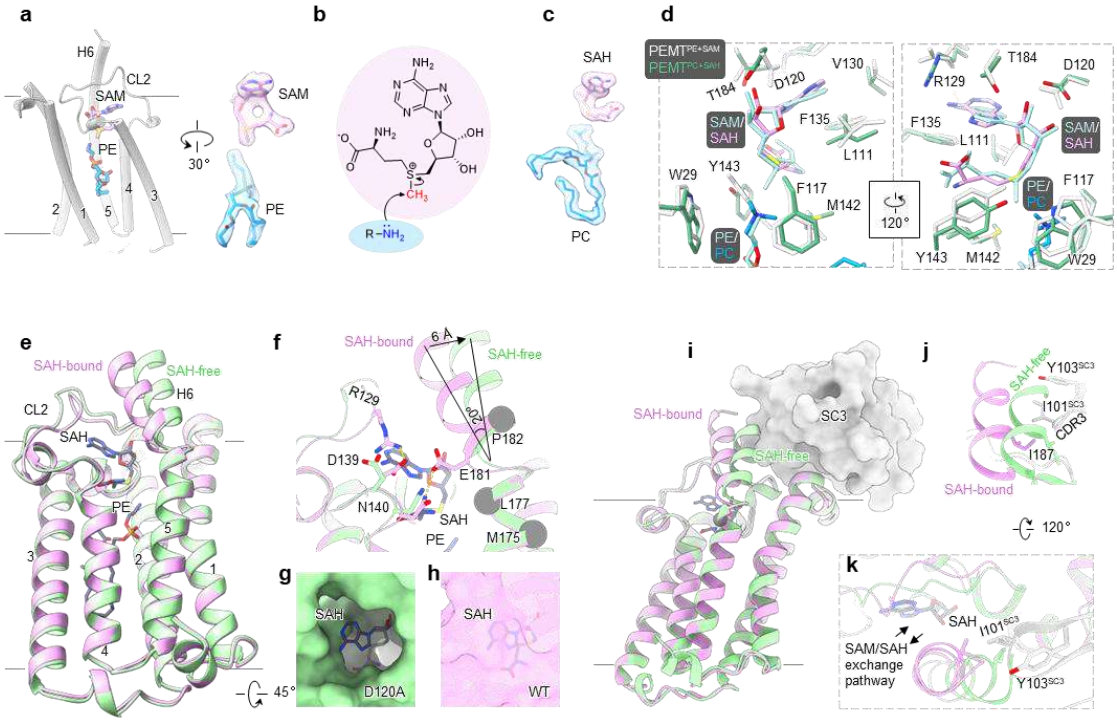


Fig. 3 | Structural basis for catalysis and SAM/SAH exchange. a Overview structure of hPEMT bound to PE (blue) and SAM (pink). Cryo-EM density for both ligands are shown on the right. **b** Proposed in-line methyl transfer mechanism. **c** Cryo-EM density of PC and SAH in the hPEMT^{PC+SAH} structure. **d** Superposition of the ligand-binding pockets in the PE/SAM-bound (white) and PC/SAH-bound (green) structures. **e–h** Structural comparison of the SAH-bound (hPEMT^{PE+SAH}; pink) and SAH-free (hPEMT^{PE}; green) states (**e, f**), showing movement of H6 and opening of the SAM/SAH exchange pathway, as visualized by surface representations (**g, h**). In **g**, SAH from hPEMT^{PE+SAH} was superimposed onto the hPEMT^{PE} structure. **i–k** Overall (**i**) and expanded (**j, k**) views showing steric clashes between the inhibitory nanobody SC3 (white) and the open hPEMT^{PE} conformation (SAH-free, green), but not the SAH-bound structure (hPEMT^{PE+SAH}; pink).

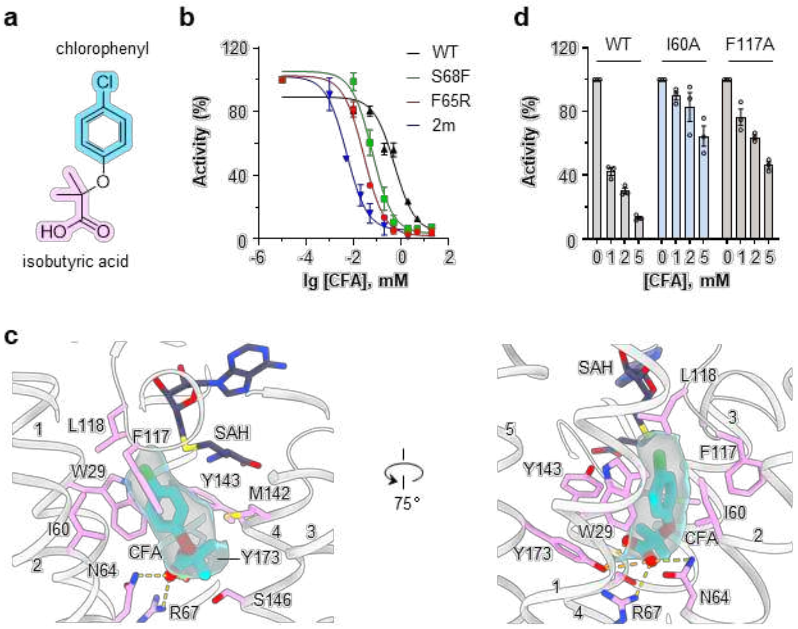


Fig. 4 | Structural basis of clofibric acid inhibition. a Chemical structure of clofibric acid (CFA). **b** IC_{50} measurements of wildtype (WT) hPEMT and the indicated mutants. **c** Interactions between CFA (cyan) and hPEMT. Interacting residues are shown as pink sticks and SAH as dark grey sticks. The cryo-EM density for CFA is shown as a semitransparent surface. Dashed lines indicate interactions within 3.4 Å. **d** Activity of hPEMT and binding-pocket mutants under varying CFA concentrations. Data in **b** and **d** represent mean ± s.e.m. from three independent experiments.

Structural mechanism of CFA inhibition

To define the molecular basis of PEMT inhibition by clofibric acid (CFA), we first characterized its effect on hPEMT activity. CFA inhibited hPEMT with an IC_{50} of 0.54 mM (**Fig. 4a, 4b**), consistent with previous measurements for rat PEMT[56,57]. Its relatively weak potency, however, prevented us from obtaining convincing CFA density in initial cryo-EM reconstructions. We therefore engineered mutations surrounding the PE-binding pocket to increase ligand occupancy. Among 46 variants tested, F65R (IC_{50} = 28 μM) and S68F (IC_{50} = 63 μM) each enhanced CFA sensitivity, whereas the combined mutant (hPEMT-2m) exhibited an approximately 100-fold lower IC_{50} (5.2 μM) than wild-type hPEMT (**Fig. 4b**). This sensitized construct enabled determination

of the CFA-bound structure at 2.66 Å resolution (hPEMT$^{CFA+SAH}$; **Fig. S9, Table S1**).

The CFA-bound structure reveals that the drug acts as a substrate-mimetic ligand, occupying the PE headgroup-binding site (**Fig. 4c**). Remarkably, the CFA scaffold closely recapitulates the positions of the PE headgroup and phosphoglycerol backbone (**Fig. S10**), allowing the inhibitor to engage the substrate-recognition network despite lacking a phospholipid headgroup. The chlorophenyl ring is nestled between the aromatic edges of Phe117 and Tyr143, which approach it from opposite sides, while the edge of the ligand is oriented toward the face of Trp29 (**Fig. 4c**), forming a three-way edge-to-face interaction network. Accommodating this geometry requires an ~40° rotation of Phe117 relative to the PE-bound structure (**Fig. S10**), a conformational change not observed between the PE- and PC-bound states (**Fig. 3d**), demonstrating an unexpected plasticity of the aromatic cage. CFA thus repurposes a binding site evolved to recognize the cationic ethanolamine headgroup for recognition of a neutral aromatic moiety. Additional interactions further stabilize the complex. Thus, Ile60 and Met142 provide hydrophobic contacts, while at the opposite end of the molecule, the carboxylate occupies the position normally taken by the phosphoglycerol moiety of PE, forming an electrostatic interaction with Arg67 and a hydrogen bond with Asn64; the two methyl substituents pack against Met142 and Tyr143 (**Fig. 4c**).

Because CFA engages residues that are themselves critical for PE recognition and catalysis, including Trp29, Tyr143, Met142, and Arg67, mutational validation of individual contacts is intrinsically constrained, as substitutions at these positions also abolished enzymatic activity (**Fig. 2b, 2d**). Nevertheless, substitution of Ile60 or Phe117 with alanine reduced CFA inhibition (**Fig. 4d**), providing functional support for the CFA-binding mode.

DISCUSSION

PEMT defines a non-canonical branch of phospholipid biosynthesis with increasingly recognized roles in liver physiology, cardiovascular health, insulin signaling, lipid metabolism, mitochondrial function, and thermogenesis[31,36,39,42,44,45]. Despite decades of cell-biology studies and earlier biochemical investigation — an experimental challenge once described as "masochistic enzymology"[31] — the molecular basis of PEMT function has remained poorly understood. Here, our structures of human PEMT provide a molecular framework for understanding its architecture, substrate recognition, catalysis, cofactor exchange, and inhibition by clofibric acid.

Pioneering kinetics studies[4] support an ordered Bi-Bi mechanism for PEMT, in which PE binds first and PC exits last. Our structures provide a structural basis for this model: the lipid-binding cavity remains occupied across the catalytic states, and the PE- and PC-bound structures show minimal differences in the lipid-binding site. Thus, substrate-to-product progression does not appear to require large-scale rearrangement of the lipid-binding cavity. Instead, PEMT catalysis occurs within a largely pre-organized active site, with the PE- and SAM-bound structure capturing the reacting groups in a geometry compatible with in-line methyl transfer. Although this configuration likely represents a near-catalytic state rather than the transition state itself, it indicates that the reacting groups are pre-positioned for chemistry. The major conformational transition observed in our structures instead involves cofactor exchange: a hinge-like rotation of helix H6 opens and closes the SAM-binding pocket, allowing PEMT to exchange soluble cofactors while maintaining its compact membrane-embedded architecture. This separation between a relatively stable lipid-binding site and a dynamic cofactor gate suggests that catalytic throughput may be modulated by the local membrane environment and cellular SAM/SAH balance without requiring major rearrangement of the active site. The extent to which additional local rearrangements or dynamic fluctuations contribute to catalysis remains unresolved.

The CFA-bound structure reveals that CFA occupies the PE-binding pocket, directly overlapping the endogenous substrate and thereby providing a structural basis for its

inhibition of PEMT. Interestingly, activation of PPARα and genetic reduction of PEMT both improve metabolic phenotypes, including protection against obesity and atherosclerosis[31-34,68]. Although these effects arise through distinct molecular mechanisms, they raise the possibility that direct inhibition of PEMT complements PPARα activation in mediating the pharmacological actions of CFA, particularly in the liver where both targets are abundant[31,68]. More broadly, CFA represents an intriguing example of how a small amphipathic carboxylic acid scaffold can engage two distinct lipid-regulatory proteins through different binding modes. However, given the relatively weak potency of CFA toward PEMT (sub-millimolar IC_{50}), the physiological contribution of this additional activity remains to be established and will likely require more selective and potent PEMT inhibitors. By identifying a chemically tractable ligand-binding pocket, the CFA-bound structure provides a structural foundation for the future development of such modulators and chemical probes.

An intriguing observation is the markedly enhanced sensitivity of the F65R/S68F mutant to CFA, despite neither residue directly contacting the inhibitor (**Fig. S10**). One possibility is that these substitutions weaken binding of the endogenous substrate PE through electrostatic and steric effects (**Fig. S10b, S10c**), thereby favoring CFA occupancy. Alternatively, they may indirectly alter the electrostatic or hydrophobic properties of the lipid-entry pathway to facilitate inhibitor binding. Importantly, because neither mutation directly participates in CFA recognition, the observed binding mode is unlikely to be substantially altered and is therefore likely to reflect the inhibition mechanism of the wild-type enzyme.

Our identification of an inhibitory nanobody highlights another strategy for modulating PEMT activity through conformational control. Although SC3 currently requires detergent conditions and is therefore not directly applicable for cellular studies, it demonstrates that PEMT activity can be regulated by stabilizing specific conformational states. The cytosolic accessibility of the regulatory region suggests that PEMT may be amenable to intracellular targeting approaches, including engineered

protein-based modulators.

Together, our structures establish the molecular basis of substrate recognition, catalysis, cofactor exchange, and inhibition of human PEMT. Beyond providing mechanistic insight into an important branch of phospholipid metabolism, these findings provide a structural framework for investigating PEMT regulation and developing selective chemical modulators for biological and biomedical applications.

REFERENCES

1 van der Veen, J. N. *et al.* The critical role of phosphatidylcholine and phosphatidylethanolamine metabolism in health and disease. *Biochimica et biophysica acta. Biomembranes* **1859**, 1558-1572 (2017).

2 Vance, D. E. Physiological roles of phosphatidylethanolamine N-methyltransferase. *Biochimica et biophysica acta* **1831**, 626-632 (2013).

3 Ridgway, N. D. & Vance, D. E. Purification of phosphatidylethanolamine N-methyltransferase from rat liver. *Journal of Biological Chemistry* **262**, 17231-17239 (1987).

4 Ridgway, N. D. & Vance, D. E. Kinetic mechanism of phosphatidylethanolamine N-methyltransferase. *The Journal of biological chemistry* **263**, 16864-16871 (1988).

5 Sadhu, M. J., Moresco, J. J., Zimmer, A. D., Yates, J. R., 3rd & Rine, J. Multiple inputs control sulfur-containing amino acid synthesis in Saccharomyces cerevisiae. *Molecular biology of the cell* **25**, 1653-1665 (2014).

6 Ye, C., Sutter, B. M., Wang, Y., Kuang, Z. & Tu, B. P. A Metabolic Function for Phospholipid and Histone Methylation. *Molecular cell* **66**, 180-193.e188 (2017).

7 Fang, W., Zhu, Y., Yang, S., Tong, X. & Ye, C. Reciprocal regulation of phosphatidylcholine synthesis and H3K36 methylation programs metabolic adaptation. *Cell reports* **39**, 110672 (2022).

8 Sharma, N. K., Langberg, K. A., Mondal, A. K. & Das, S. K. Phospholipid biosynthesis genes and susceptibility to obesity: analysis of expression and polymorphisms. *PloS one* **8**, e65303 (2013).

9 Su, G. M. *et al.* Association between PEMT rs7946 and blood pressure levels in Chinese adolescents. *Blood Pressure Monitoring* **29** (2024).

10 Tajuddin, S. M. *et al.* LINE-1 methylation in leukocyte DNA, interaction with phosphatidylethanolamine N-methyltransferase variants and bladder cancer risk. *British journal of cancer* **110**, 2123-2130 (2014).

11 Xu, X. *et al.* Choline metabolism and risk of breast cancer in a population-based study. *FASEB journal : official publication of the Federation of American Societies for Experimental Biology* **22**, 2045-2052 (2008).

12 He, Q. *et al.* The Mediating Effect of the Choline-to-Betaine Ratio on the Association Between PEMT rs7946 and Digestive System Cancer: A Nested Case-Control Study in a Chinese Population. *Curr Dev Nutr* **8**, 102075 (2024).

13 Zinrajh, D. *et al.* Increased phosphatidylethanolamine N-methyltransferase gene expression in non-small-cell lung cancer tissue predicts shorter patient survival. *Oncology letters* **7**, 2175-2179 (2014).

14 Zhu, J. *et al.* Dietary Choline Intake during Pregnancy and PEMT rs7946 Polymorphism on Risk of Preterm Birth: A Case-Control Study. *Annals of nutrition & metabolism* **76**, 431-440 (2020).

15 Zhang, J. *et al.* Phosphatidylethanolamine N-methyltransferase (PEMT) gene polymorphisms and risk of spina bifida. *American journal of medical genetics. Part A* **140**, 785-789 (2006).

16 Bale, G. *et al.* Whole-Exome Sequencing Identifies a Variant in Phosphatidylethanolamine N-Methyltransferase Gene to be Associated With Lean-Nonalcoholic Fatty Liver Disease. *Journal of clinical and experimental hepatology* **9**, 561-568 (2019).

17 Jun, D. W. *et al.* Polymorphisms of microsomal triglyceride transfer protein gene and phosphatidylethanolamine N-methyltransferase gene in alcoholic and nonalcoholic fatty liver disease in Koreans. *European journal of gastroenterology & hepatology* **21**, 667-672 (2009).

18 Tan, H. L., Mohamed, R., Mohamed, Z. & Zain, S. M. Phosphatidylethanolamine N-

methyltransferase gene rs7946 polymorphism plays a role in risk of nonalcoholic fatty liver disease: evidence from meta-analysis. *Pharmacogenetics and genomics* **26**, 88-95 (2016).

19 Song, J. *et al.* Polymorphism of the PEMT gene and susceptibility to nonalcoholic fatty liver disease (NAFLD). *FASEB journal : official publication of the Federation of American Societies for Experimental Biology* **19**, 1266-1271 (2005).

20 Dong, H. *et al.* The phosphatidylethanolamine N-methyltransferase gene V175M single nucleotide polymorphism confers the susceptibility to NASH in Japanese population. *Journal of hepatology* **46**, 915-920 (2007).

21 Zeisel, S. H. People with fatty liver are more likely to have the PEMT rs7946 SNP, yet populations with the mutant allele do not have fatty liver. *The FASEB Journal* **20**, 2181-2182 (2006).

22 Zhou, Y. J. *et al.* Influence of polygenetic polymorphisms on the susceptibility to non-alcoholic fatty liver disease of Chinese people. *J Gastroenterol Hepatol* **25**, 772-777 (2010).

23 Ridgway, N. D. & Vance, D. E. Specificity of rat hepatic phosphatidylethanolamine N-methyltransferase for molecular species of diacyl phosphatidylethanolamine. *The Journal of biological chemistry* **263**, 16856-16863 (1988).

24 Pynn, C. J. *et al.* Specificity and rate of human and mouse liver and plasma phosphatidylcholine synthesis analyzed in vivo. *Journal of lipid research* **52**, 399-407 (2011).

25 Watkins, S. M., Zhu, X. & Zeisel, S. H. Phosphatidylethanolamine-N-methyltransferase activity and dietary choline regulate liver-plasma lipid flux and essential fatty acid metabolism in mice. *The Journal of nutrition* **133**, 3386-3391 (2003).

26 da Costa, K. A. *et al.* Dietary docosahexaenoic acid supplementation modulates hippocampal development in the Pemt-/- mouse. *The Journal of biological chemistry* **285**, 1008-1015 (2010).

27 Guan, Z. Z., Wang, Y. N., Xiao, K. Q., Hu, P. S. & Liu, J. L. Activity of phosphatidylethanolamine-N-methyltransferase in brain affected by Alzheimer's disease. *Neurochemistry international* **34**, 41-47 (1999).

28 Serafim, V. *et al.* Single Nucleotide Polymorphisms in PEMT and MTHFR Genes are Associated with Omega 3 and 6 Fatty Acid Levels in the Red Blood Cells of Children with Obesity. *Nutrients* **11** (2019).

29 Amarsi, R. *et al.* A co-ordinated transcriptional programme in the maternal liver supplies long chain polyunsaturated fatty acids to the conceptus using phospholipids. *Nature communications* **15**, 6767 (2024).

30 Mun, J. G., Legette, L. L., Ikonte, C. J. & Mitmesser, S. H. Choline and DHA in Maternal and Infant Nutrition: Synergistic Implications in Brain and Eye Health. *Nutrients* **11** (2019).

31 Vance, D. E. From masochistic enzymology to mechanistic physiology and disease. *The Journal of biological chemistry* **292**, 17169-17177 (2017).

32 Jacobs, R. L. *et al.* Impaired de novo choline synthesis explains why phosphatidylethanolamine N-methyltransferase-deficient mice are protected from diet-induced obesity. *The Journal of biological chemistry* **285**, 22403-22413 (2010).

33 Zhao, Y. *et al.* Lack of phosphatidylethanolamine N-methyltransferase alters plasma VLDL phospholipids and attenuates atherosclerosis in mice. *Arteriosclerosis, thrombosis, and vascular biology* **29**, 1349-1355 (2009).

34 Watanabe, M. *et al.* Pemt deficiency ameliorates endoplasmic reticulum stress in diabetic nephropathy. *PloS one* **9**, e92647 (2014).

35 Noga, A. A., Zhao, Y. & Vance, D. E. An unexpected requirement for phosphatidylethanolamine

N-methyltransferase in the secretion of very low density lipoproteins. *The Journal of biological chemistry* **277**, 42358-42365 (2002).

36 van der Veen, J. N. *et al.* A role for phosphatidylcholine and phosphatidylethanolamine in hepatic insulin signaling. *FASEB journal : official publication of the Federation of American Societies for Experimental Biology* **33**, 5045-5057 (2019).

37 Gao, X. *et al.* Decreased lipogenesis in white adipose tissue contributes to the resistance to high fat diet-induced obesity in phosphatidylethanolamine N-methyltransferase-deficient mice. *Biochimica et biophysica acta* **1851**, 152-162 (2015).

38 van der Veen, J. N., Lingrell, S., da Silva, R. P., Jacobs, R. L. & Vance, D. E. The concentration of phosphatidylethanolamine in mitochondria can modulate ATP production and glucose metabolism in mice. *Diabetes* **63**, 2620-2630 (2014).

39 Ayer, A. *et al.* Genetic screening reveals phospholipid metabolism as a key regulator of the biosynthesis of the redox-active lipid coenzyme Q. *Redox biology* **46**, 102127 (2021).

40 Shields, D. J., Lingrell, S., Agellon, L. B., Brosnan, J. T. & Vance, D. E. Localization-independent regulation of homocysteine secretion by phosphatidylethanolamine N-methyltransferase. *The Journal of biological chemistry* **280**, 27339-27344 (2005).

41 Noga, A. A. *et al.* Plasma homocysteine is regulated by phospholipid methylation. *The Journal of biological chemistry* **278**, 5952-5955 (2003).

42 Presa, N., Dominguez-Herrera, A., van der Veen, J. N., Vance, D. E. & Gómez-Muñoz, A. Implication of phosphatidylethanolamine N-methyltransferase in adipocyte differentiation. *Biochimica et biophysica acta. Molecular basis of disease* **1866**, 165853 (2020).

43 Hörl, G. *et al.* Sequential synthesis and methylation of phosphatidylethanolamine promote lipid droplet biosynthesis and stability in tissue culture and in vivo. *The Journal of biological chemistry* **286**, 17338-17350 (2011).

44 Verkerke, A. R. P. *et al.* Phospholipid methylation regulates muscle metabolic rate through Ca(2+) transport efficiency. *Nature metabolism* **1**, 876-885 (2019).

45 Wan, S. *et al.* Impaired Hepatic Phosphatidylcholine Synthesis Leads to Cholestasis in Mice Challenged With a High-Fat Diet. *Hepatology communications* **3**, 262-276 (2019).

46 Walkey, C. J., Yu, L., Agellon, L. B. & Vance, D. E. Biochemical and evolutionary significance of phospholipid methylation. *The Journal of biological chemistry* **273**, 27043-27046 (1998).

47 Ling, J., Chaba, T., Zhu, L. F., Jacobs, R. L. & Vance, D. E. Hepatic ratio of phosphatidylcholine to phosphatidylethanolamine predicts survival after partial hepatectomy in mice. *Hepatology (Baltimore, Md.)* **55**, 1094-1102 (2012).

48 Tessitore, L., Dianzani, I., Cui, Z. & Vance, D. E. Diminished expression of phosphatidylethanolamine N-methyltransferase 2 during hepatocarcinogenesis. *The Biochemical journal* **337 (Pt 1)**, 23-27 (1999).

49 Tessitore, L., Sesca, E. & Vance, D. E. Inactivation of phosphatidylethanolamine N-methyltransferase-2 in aflatoxin-induced liver cancer and partial reversion of the neoplastic phenotype by PEMT transfection of hepatoma cells. *Int J Cancer* **86**, 362-367 (2000).

50 Marengo, B., Bottini, C., La Porta, C. A., Domenicotti, C. & Tessitore, L. Inactivation of PEMT2 in hepatocytes initiated by DENA in fasted/refed rats. *Biochemical and biophysical research communications* **346**, 234-241 (2006).

51 Duce, A. M., Ortíz, P., Cabrero, C. & Mato, J. M. S-adenosyl-L-methionine synthetase and phospholipid methyltransferase are inhibited in human cirrhosis. *Hepatology (Baltimore, Md.)* **8**,

65-68 (1988).
52 Tessitore, L. *et al.* Expression of phosphatidylethanolamine N-methyltransferase in human hepatocellular carcinomas. *Oncology* **65**, 152-158 (2003).
53 van der Veen, J. N. *et al.* Fenofibrate, but not ezetimibe, prevents fatty liver disease in mice lacking phosphatidylethanolamine N-methyltransferase. *Journal of lipid research* **58**, 656-667 (2017).
54 Veen, J. N. v. d. *et al.* Pioglitazone attenuates hepatic inflammation and fibrosis in phosphatidylethanolamine N-methyltransferase-deficient mice. *American Journal of Physiology-Gastrointestinal and Liver Physiology* **310**, G526-G538 (2016).
55 Presa, N. *et al.* Vitamin E alleviates non-alcoholic fatty liver disease in phosphatidylethanolamine N-methyltransferase deficient mice. *Biochimica et biophysica acta. Molecular basis of disease* **1865**, 14-25 (2019).
56 Nishimaki-Mogami, T., Suzuki, K., Okochi, E. & Takahashi, A. Bezafibrate and clofibric acid are novel inhibitors of phosphatidylcholine synthesis via the methylation of phosphatidylethanolamine. *Biochimica et biophysica acta* **1304**, 11-20 (1996).
57 Nishimaki-Mogami, T., Yao, Z. & Fujimori, K. Inhibition of phosphatidylcholine synthesis via the phosphatidylethanolamine methylation pathway impairs incorporation of bulk lipids into VLDL in cultured rat hepatocytes. *Journal of lipid research* **43**, 1035-1045 (2002).
58 Mizuguchi, H., Kudo, N. & Kawashima, Y. Metabolic alterations by clofibric acid in the formation of molecular species of phosphatidylcholine in rat liver. *Biochem Pharmacol* **62**, 853-861 (2001).
59 Nishimaki-Mogami, T., Suzuki, K. & Takahashi, A. The role of phosphatidylethanolamine methylation in the secretion of very low density lipoproteins by cultured rat hepatocytes: rapid inhibition of phosphatidylethanolamine methylation by bezafibrate increases the density of apolipoprotein B48-containing lipoproteins. *Biochimica et biophysica acta* **1304**, 21-31 (1996).
60 Morita, S. Y., Takeuchi, A. & Kitagawa, S. Functional analysis of two isoforms of phosphatidylethanolamine N-methyltransferase. *The Biochemical journal* **432**, 387-398 (2010).
61 Morita, S. Y. *et al.* Effects of phosphatidylethanolamine N-methyltransferase on phospholipid composition, microvillus formation and bile salt resistance in LLC-PK1 cells. *Febs j* **278**, 4768-4781 (2011).
62 Wu, X. & Rapoport, T. A. Cryo-EM structure determination of small proteins by nanobody-binding scaffolds (Legobodies). *Proc Natl Acad Sci U S A* **118** (2021).
63 Zimmermann, I. *et al.* Synthetic single domain antibodies for the conformational trapping of membrane proteins. *eLife* **7**, e34317 (2018).
64 Kim, S. *et al.* Transmembrane glycine zippers: physiological and pathological roles in membrane proteins. *Proc Natl Acad Sci U S A* **102**, 14278-14283 (2005).
65 Xiong, Q. *et al.* Molecular architecture of human LYCHOS involved in lysosomal cholesterol signaling. *Nat Struct Mol Biol* **32**, 905-913 (2025).
66 Shields, D. J., Altarejos, J. Y., Wang, X., Agellon, L. B. & Vance, D. E. Molecular dissection of the S-adenosylmethionine-binding site of phosphatidylethanolamine N-methyltransferase. *The Journal of biological chemistry* **278**, 35826-35836 (2003).
67 Nelson, D. L., Lehninger, A. L. & Cox, M. M. *Lehninger Principles of Biochemistry*. (W. H. Freeman, 2008).
68 Gross, B., Pawlak, M., Lefebvre, P. & Staels, B. PPARs in obesity-induced T2DM, dyslipidaemia and NAFLD. *Nature Reviews Endocrinology* **13**, 36-49 (2017).
69 Cai, H. *et al.* An improved fluorescent tag and its nanobodies for membrane protein expression,

stability assay, and purification. *Communications Biology* **3**, 753 (2020).

70 Cai, H., Yao, H., Li, T., Tang, Y. & Li, D. High-level heterologous expression of the human transmembrane sterol Δ8,Δ7-isomerase in Pichia pastoris. *Protein Expr Purif* **164**, 105463 (2019).

71 Li, T. *et al.* Uncovering a conserved vulnerability site in SARS-CoV-2 by a human antibody. *EMBO Mol Med* **13**, e14544 (2021).

72 Nasr, M. L. *et al.* Covalently circularized nanodiscs for studying membrane proteins and viral entry. *Nat Methods* **14**, 49-52 (2017).

73 Emsley, P., Lohkamp, B., Scott, W. G. & Cowtan, K. Features and development of Coot. *Acta Crystallogr D Biol Crystallogr* **66**, 486-501 (2010).

74 Adams, P. D. *et al.* PHENIX: a comprehensive Python-based system for macromolecular structure solution. *Acta Crystallogr D Biol Crystallogr* **66**, 213-221 (2010).

75 Meng, E. C. *et al.* UCSF ChimeraX: Tools for structure building and analysis. *Protein Sci* **32**, e4792 (2023).

METHODS

Molecular cloning

DNA encoding hPEMT was amplified from a human cDNA library and cloned into the pBTSG[69] vector using *BamH*I and *Kpn*I restriction sites. A C-terminal thermostable GFP (TGP) tag was fused to hPEMT through a human rhinovirus (HRV) 3C protease cleavage site, followed by a Strep II affinity tag. For sybody selection, an Avi-tag (GLNDIFEAQKIEWHE) was inserted between hPEMT and the 3C cleavage site by polymerase chain reaction (PCR). The soluble phosphatidylethanolamine methyltransferase (PmtA) from *Rubellimicrobium thermophilum* (GenBank: WP_021097699.1) was codon optimized, synthesized (Azanda, China), and cloned into the p3EC[70] vector using *BamH*I and *Kpn*I restriction sites. An N-terminal maltose-binding protein (MBP) fusion was introduced to improve protein solubility. All point mutations were generated by site-directed PCR and verified by Sanger sequencing.

Expression and small-scale purification of hPEMT variants

hPEMT mutants were transiently expressed in Expi293 cells using polyethyleneimine (PEI)-mediated transfection. Cells were cultured at 37 °C and transfected at a density of 2×10^6 cells mL^{-1} with 24 μg plasmid DNA and 72 μg PEI per 24 mL culture in the presence of 2 mM valproic acid (VPA). Cells were harvested 60 h after transfection by centrifugation (1,500 × g, 5 min), flash-frozen in liquid nitrogen, and stored at -80 °C.

All purification procedures were performed at 4 °C. Cell pellets (~0.3 g) were solubilized for 1.5 h in buffer containing 1% LMNG, 150 mM NaCl, 50 mM Tris-HCl (pH 8.0), 1 mM dithiothreitol (DTT), 1 mM ethylenediaminetetraacetic acid (EDTA), protease inhibitor cocktail, DNase I (10 μg mL^{-1}), and 8 mM $MgCl_2$. Insoluble material was removed by centrifugation (21,000 × g, 1 h), and the supernatant was incubated with Strep-Tactin resin for 2 h. After washing once with high-salt buffer (1 M NaCl, 0.01% LMNG, 0.2 mM tris(2-carboxyethyl)phosphine (TCEP), 50 mM Tris-HCl, pH 8.0) and twice with low-salt buffer (150 mM NaCl, 0.01% LMNG, 0.2 mM TCEP, 50 mM Tris-HCl, pH 8.0), proteins were eluted with 5 mM D-desthiobiotin in low-salt

buffer, flash-frozen in liquid nitrogen, and stored at -80 °C.

Activity assay

PE (Cat. 850757P, Avanti) was dissolved in chloroform, dried under a stream of argon, and lyophilized under high vacuum (FreeZone 2.5L, Labconco) for 4 h. The dried lipid film was resuspended by sonication (15 min) in 1 mM Triton X-100, 50 mM Tris-HCl (pH 9.2), 1 mM EDTA, and 0.4 mM TCEP to yield a final PE concentration of 4 mM (80 mol% relative to Triton X-100). Standard activity assays were performed in 20 µL reactions containing 2 mM PE, purified hPEMT (1 µg mL^{-1} for the wild-type enzyme; 10 µg mL^{-1} for some loss-of-function mutants), and 30 µM [^{3}H]-SAM (0.167 Ci $mmol^{-1}$) in 50 mM Tris-HCl (pH 9.2). Reactions were initiated by addition of SAM and incubated at 25 °C for 30 min, a time interval over which product formation was linear with both incubation time and enzyme concentration (0.2–160 µg mL^{-1}). Reactions were terminated by adding 200 µL chloroform (1:1, v/v) followed by 500 µL water. After vortexing and centrifugation (12,000 × g, 2 min), the aqueous phase was discarded and the organic phase was washed twice with water to remove unreacted [^{3}H]-SAM. The organic solvent was evaporated, and the extracted lipids were resuspended in 500 µL scintillation cocktail (Cat. 1200.437, Revvity). Radioactivity was measured using a Tri-Carb 5110TR liquid scintillation counter (PerkinElmer). For kinetic analysis, SAM concentrations were varied between 0.2 and 20 µM while maintaining 2 mM PE and 0.5 µg mL^{-1} purified hPEMT. Apparent K_m and V_{max} values were obtained by nonlinear regression using GraphPad Prism 9. For assays in LMNG, PE and LMNG (4:10 molar ratio) were mixed in chloroform, dried under argon, lyophilized, and resuspended in Milli-Q water to produce a 40 mM PE stock. Reactions were performed as described above except that LMNG replaced Triton X-100 and were incubated at room temperature (20–25 °C). CFA inhibition assays were carried out in LMNG in the presence of 2 mM PE and 1 mM SAM. For assay in nanodisc, nanodisc-reconsituted hPEMT (see below) was included at 2 µg mL^{-1} and SAM was included at 30 µM. Lipid extraction and radioactivity measurements were carried out as described for the Triton X-100 assay.

Purification and biotinylation of Avi-tagged hPEMT

Unless otherwise stated, all purification steps were performed at 4 °C. Cell pellets from 1 L of Expi293 culture expressing Avi-tagged hPEMT were resuspended in 40 mL lysis buffer containing 10% glycerol, 1 mM DTT, 1 mM phenylmethylsulfonyl fluoride (PMSF), 1 mM EDTA, protease inhibitor cocktail, DNase I (10 μg mL^{-1}), and 8 mM $MgCl_2$, 150 mM NaCl, 50 mM Tris-HCl (pH 8.0). Cells were disrupted by sonication using a 10-mm probe (30% amplitude, 1-s on/2-s off, 5 min), and the membrane fraction was collected by centrifugation at 48,000 × *g* for 1 h. Membranes were resuspended in storage buffer (1 mM PMSF, 40% glycerol, 150 mM NaCl, 50 mM Tris-HCl pH 8.0), flash-frozen in liquid nitrogen, and stored at -80 °C. Membrane pellets were resuspended in three volumes of buffer containing 150 mM NaCl, 1 mM PMSF, 1 × protein inhibitor cocktail, and 50 mM Tris-HCl pH 8.0, followed by solubilization with 1% LMNG for 2 h. Insoluble material was removed by centrifugation at 48,000 × *g* for 1 h. The supernatant was incubated with Strep-Tactin resin for 2 h, and the resin was transferred to a gravity column. After washing with 7 column volumes (CV) of 1 M NaCl, 0.01% LMNG, 0.2 mM TCEP, 10% glycerol, 50 mM Tris-HCl, pH 8.0, followed by 7 CV of 150 mM NaCl, 0.01% LMNG, 0.2 mM TCEP, 10% glycerol, 50 mM Tris-HCl, pH 8.0, protein was eluted with 5 mM D-desthiobiotin in the buffer above. The eluate was desalted using a desalting column (Cat. 732-2010, Bio-Rad).

For enzymatic biotinylation, purified hPEMT (9.5 μM) was incubated with 15 μM biotin, 10 mM magnesium acetate, 5 mM ATP, and home-purified BirA (16.7 μg mL^{-1}) in a final volume of 3.6 mL at 4 °C for 16 h. HRV 3C protease was added simultaneously to remove the C-terminal TGP tag. The reaction mixture was subsequently passed over Strep-Tactin resin to remove the cleaved TGP tag. Biotinylated hPEMT was concentrated and further purified by size-exclusion chromatography on a Superose 6 Increase 10/300 GL column preequilibrated in Low-Salt Buffer. Peak fractions were concentrated, flash-frozen in liquid nitrogen, and stored at -80 °C.

Sybody selection

Three synthetic sybody libraries[63] (Concave, Loop, and Convex) were translated *in*

vitro using the PUREfrex 2.1 kit. Briefly, 4 µL Solution I, 0.5 µL Solution II, 1 µL Solution III, 0.5 µL of 10 mM cysteine, 0.5 µL of 80 mM reduced glutathione, 0.5 µL of 60 mM oxidized glutathione, 0.5 µL of 1.875 mg mL^{-1} disulfide bond isomerase DsbC (DS supplement, Cat. PF005-0.5-EX, GeneFrontier), and 1.8 µL nuclease-free water were pre-incubated at 37 °C for 5 min. Subsequently, 0.7 µL of the mRNA library was added, and *in vitro* translation was carried out at 37 °C for 30 min. The resulting mix were diluted into 100 µL panning buffer containing 0.5% bovine serum albumin (BSA), 0.1% LMNG, 150 mM NaCl, 50 mM magnesium acetate, 0.5% heparin, 1 µL RNaseIn, and 50 mM Tris-acetate (pH 7.4), followed by centrifugation at 21,000 × *g* for 5 min. The supernatant was incubated with 50 nM biotinylated hPEMT on ice for 20 min and subsequently mixed with 12 µL Dynabeads MyOne Streptavidin T1 (Thermo Fisher Scientific) pre-equilibrated in panning buffer. After capture of hPEMT-bound ribosome complexes, bound mRNA was eluted with 100 µg mL^{-1} yeast RNA, reverse-transcribed into cDNA using reverse transcriptase (Cat. 200436, Agilent), purified using a DNA purification kit (Cat. A740609.25, Macherey-Nagel), and amplified using GoTaq G2 DNA polymerase. PCR products were gel purified, digested with *BspQ*I, ligated into the pDX_init vector[63] using T4 DNA ligase, and transformed into *E. coli* SS320 by electroporation for phage display. Two rounds of phage display were subsequently performed. For the first round, 96-well plates coated overnight with 67 nM neutravidin (Cat. 31000, Thermo Fisher Scientific) were used for target immobilization. Phage particles displaying sybodies were incubated with 50 nM biotinylated hPEMT and washed with TBS buffer (150 mM NaCl, 50 mM Tris-HCl, pH 7.4) containing 0.1% LMNG and 0.5% BSA. Bound phages were eluted with 0.25 mg mL^{-1} trypsin in TBS buffer and naamplified. The second round of selection was carried out in 1.5-mL low-binding tubes using 12 µL Dynabeads MyOne Streptavidin C1. Following incubation with 50 nM biotinylated hPEMT, phages were challenged with 5 µM non-biotinylated hPEMT to compete away weak binders. After two rounds of selection, enriched phagemids were subcloned into the pSb_init vector by FX cloning for soluble expression in *E. coli* MC1061.

Sybody selection was repeated using hPMET reconstituted into nanodiscs. The procedures were the same except that 1) an additional phage display step was performed with 5 nM biotinylated hPEMT for binding and 500 nM non-biotinylated hPEMT for counter selection; and 2) the nanodisc-reconstituted hPEMT was used in the ribosome display, and the last two phage display steps.

Enzyme-Linked Immunosorbent Assay (ELISA) screening of sybodies

Individual *E. coli* MC1061 transformants were inoculated into 96-deep-well plates and cultured at 37 °C with shaking at 300 rpm for 4 h. Cultures were diluted 1:20 into 1 mL Terrific Broth supplemented with 25 μg mL^{-1} antibiotic and grown for an additional 2 h at 37 °C, followed by 1.5 h at 22 °C before induction with 0.02% (w/v) arabinose. Protein expression proceeded for 16 h at 22 °C with shaking at 300 rpm. Cells were harvested by centrifugation at 3,220 × *g* for 30 min and resuspended in 0.1 mL TES buffer (20% sucrose, 0.5 mM EDTA, 50 mM Tris-HCl, pH 8.0). After incubation at room temperature (RT, 21-25 °C) for 30 min, periplasmic proteins were released by addition of 0.9 mL TBS buffer containing 1 mM $MgCl_2$. Following centrifugation at 3,220 × *g* for 30 min, the supernatant was collected for ELISA analysis. For ELISA screening, MaxiSorp 96-well plates (Cat. 442404, Thermo Fisher Scientific) were coated overnight with protein A at 4 °C. Plates were washed with TBS buffer, blocked with 0.5% BSA in TBS buffer for 30 min at room temperature, and washed three times with TBS buffer. Anti-Myc antibody (Cat. M4439, Sigma) diluted 1:2,000 in TBS-BSA-D buffer (0.5% BSA, 0.1% LMNG in TBS) was added and incubated for 20 min at room temperature. After three washes with TBS-D buffer (0.008% LMNG in TBS), periplasmic extracts containing Myc-tagged sybodies were added and incubated for 20 min. Plates were washed again, followed by incubation with 50 nM biotinylated hPEMT or an unrelated control protein for 20 min. After three additional washes, streptavidin-HRP (Cat. S2438, Sigma), diluted 1:5,000 in TBS-BSA-D buffer, was added and incubated for 20 min. Plates were washed three times with TBS-D buffer before addition of freshly prepared ELISA developing solution containing 50 mM Na_2HPO_4, 24 mM citric acid, 0.006% H_2O_2, and 0.1 mg mL^{-1} 3,3′,5,5′-

tetramethylbenzidine. Absorbance at 650 nm was measured using an M2e plate reader (Molecular Devices).

Expression and purification of Fab8D3-2

DNA encoding the light chain and C-terminal His-tagged heavy chain of Fab8D3-2[62] was cloned into the pDEC vector[71]. Expi293 cells (2×10^6 cells mL^{-1}) were co-transfected with the two plasmids (0.5 mg L^{-1} each) using linear polyethyleneimine (3 mg L^{-1}). Sodium butyrate was added to a final concentration of 10 mM 10–12 h after transfection to enhance protein expression, and the cells were cultured for an additional 60 h. The culture medium containing secreted Fab was harvested by centrifugation and filtered through a 0.22-μm membrane. The clarified medium was supplemented with 5 mM imidazole, 150 mM NaCl, and 50 mM Tris-HCl (pH 8.0), followed by incubation with Ni-Sepharose resin (GE Healthcare) overnight at 4 °C. The resin was packed into a gravity-flow column, washed with 20 column volumes (CV) of **Buffer A** (150 mM NaCl, 20 mM Tris-HCl pH 8.0) supplemented with 10 mM imidazole, and the protein was eluted with 300 mM imidazole in Buffer A. Eluted protein was aliquoted, flash-frozen in liquid nitrogen, and stored at -80 °C. Protein concentration was determined from absorbance at 280 nm using a theoretical extinction coefficient of 80,385 M^{-1} cm^{-1}.

Expression and purification of MBP-PrA/G

DNA encoding MBP-PrA/G[62] with a C-terminal 8×His tag was cloned into the pET22a vector. The plasmid was transformed into *E. coli* BL21(DE3). Cells were grown in Luria-Bertani (LB) medium supplemented with 50 μg mL^{-1} kanamycin at 37 °C with shaking (220 rpm) to an OD_{600} of ~0.6, induced with 1 mM isopropyl β-d-1-thiogalactopyranoside (IPTG), and cultured for an additional 4 h. Cells were harvested and resuspended in Lysis Buffer (400 mM NaCl, 20 mM imidazole, 50 mM HEPES pH 7.5) supplemented with 5 mM $MgCl_2$, 10 μg mL^{-1} DNase I, and 1 mM PMSF before lysis using a high-pressure homogenizer. Cell debris was removed by centrifugation at 25,000 × *g* for 30 min. The clarified lysate was incubated with Ni-NTA resin pre-equilibrated in Lysis Buffer for 3 h at 4 °C. After washing with 20 CV of Lysis Buffer,

bound protein was eluted with 300 mM imidazole in Buffer B (150 mM NaCl, 20 mM HEPES pH 7.5). The eluate was further purified by size-exclusion chromatography on a Superdex 200 Increase 10/300 GL column equilibrated in Buffer B supplemented with 5% (v/v) glycerol. Peak fractions were pooled, aliquoted, flash-frozen in liquid nitrogen, and stored at -80 °C. Protein concentration was determined from absorbance at 280 nm using a theoretical extinction coefficient of 77,810 M^{-1} cm^{-1}.

Expression and purification of Sybody

Sybodies used for legobody assembly were modified by site-directed PCR according to the published legobody design and expressed with a C-terminal His tag in *E. coli* MC1061. Cells carrying pSb-init constructs were grown in Terrific Broth supplemented with 25 μg mL^{-1} chloramphenicol at 37 °C with shaking (220 rpm) to an OD_{600} of approximately 0.5. Cultures were shifted to 22 °C, grown for an additional 1.5 h, and induced with 0.02% (w/v) arabinose for 17 h. Periplasmic proteins were extracted by osmotic shock. Briefly, cells from 1 L of culture were resuspended in 20 mL TES-high Buffer (0.5 M sucrose, 0.5 mM EDTA, and 0.2 M Tris-HCl pH 8.0) and incubated at 4 °C for 30 min before addition of 40 mL ice-cold Milli-Q water and incubation for a further 1 h. The periplasmic fraction was collected by centrifugation at 25,000 × *g* for 30 min. The supernatant was adjusted to contain 150 mM NaCl, 2 mM $MgCl_2$, and 20 mM imidazole before incubation with pre-equilibrated Ni-NTA resin for 2 h. After washing with buffer containing 30 mM imidazole, sybodies were eluted with 300 mM imidazole in Buffer A. Purified proteins were either used immediately or flash-frozen in liquid nitrogen and stored at -80 °C.

Assembly and purification of legobodies

Legobody complexes were assembled by first mixing MBP-PrA/G with Fab8D3-2 at a molar ratio of 1:1.1. A desired sybody was then added at a threefold molar excess over MBP-PrA/G, and the mixture was incubated on ice for 30 min. The assembled complexes were captured on amylose resin (Cat. E8021V, New England Biolabs). After batch binding for 1 h at 4 °C, the resin was washed with 6 CV of Buffer C (150 mM

NaCl, 50 mM Tris-HCl pH 8.0) supplemented with 1 mM EDTA, and the legobody complex was eluted with 20 mM maltose in Buffer C. Freshly purified legobody was used immediately for PEMT complex assembly.

Purification and legobody assembly of nanodisc-reconstituted PEMT

Membrane suspensions (4 mL) were diluted with an equal volume of buffer containing 150 mM NaCl and 50 mM HEPES pH 7.5 supplemented with 0.2 mM TCEP, 1× protease inhibitor cocktail, and 2 mg mL^{-1} iodoacetamide, and the suspension was incubated for 30 min before solubilization. Subsequently, an equal volume of solubilization buffer containing 2% *n*-dodecyl β-D-maltoside (DDM), 0.2 mM TCEP, 1× protease inhibitor cocktail, 150 mM NaCl, and 50 mM HEPES (pH 7.5) was added, and the mixture was gently rotated for 1 h. Insoluble material was removed by centrifugation at 48,000 × *g* for 1 h. The clarified supernatant was incubated with 2 mL Strep-Tactin resin for 1 h, and the resin was transferred to a gravity-flow column. The column was washed with 3 CV Wash Buffer 1 (0.03% DDM, 0.01% LMNG, 0.2 mM TCEP, 150 mM NaCl, 50 mM HEPES pH 7.5), followed by 1.5 CV Wash Buffer 2 (0.1% LMNG, 0.2 mM TCEP, 150 mM NaCl, 50 mM HEPES pH 7.5). After a 10-min incubation, the column was further washed with an additional 1.5 CV Wash Buffer 2 and 3 CV Wash Buffer 3 (0.01% LMNG, 0.2 mM TCEP, 150 mM NaCl, 50 mM HEPES pH 7.5). Bound protein was eluted with 5 mM D-desthiobiotin in Wash Buffer 3 and desalted into buffer containing 0.01% LMNG, 0.2 mM TCEP, 150 mM NaCl, and 50 mM HEPES (pH 7.5) using a desalting column. The desalted protein was reconstituted into nanodiscs by mixing hPEMT, NW9 scaffold protein[72], and lipids (PE:PS = 1:9, mol/mol) at a molar ratio of 1:4:200. The mixture was incubated for 2 h, after which preassembled LB11 legobody was added at a molar ratio of 1:1.5 relative to hPEMT. Nanodisc assembly was initiated by sequential addition of Bio-Beads to a final concentration of 200 mg mL^{-1} and allowed to proceed overnight with gentle rotation. The following day, assembled PEMT-nanodisc-legobody complexes were captured by batch binding to approximately 0.7 mL Strep-Tactin resin for 1 h to remove free nanodiscs and excess legobody. After washing with 5 CV SEC buffer (0.2 mM TCEP,

2 mM maltose, 150 mM NaCl, 20 mM HEPES pH 7.5), the complexes were eluted with 5 mM D-desthiobiotin in SEC buffer and further purified by size-exclusion chromatography on a Superose 6 Increase 10/300 GL column equilibrated in SEC buffer. Peak fractions corresponding to the PEMT-legobody complex were pooled and concentrated to 11.6 mg mL^{-1} for cryo-EM sample preparation. Protein concentration was determined from absorbance at 493 nm using a theoretical extinction coefficient of 64,220 M^{-1} cm^{-1}.

The D120A mutant was purified using the same procedure as wild-type hPEMT, and the final cryo-EM sample was concentrated to 7.2 mg mL^{-1}. For purification of the $hPEMT^{2m}$ mutant, 5 mM clofibric acid (CFA) was included throughout purification and size-exclusion chromatography. Peak fractions were concentrated to 5.2 mg mL^{-1}.

Purification and legobody assembly of PEMT complexes in detergents

To capture hPEMT with both substrates (PE and SAM), membrane suspensions were diluted in Buffer A supplemented with 10 μM SC3 (the inhibitory sybody, IC_{50} = 83 nM), 1 mM SAM, 0.2 mM TCEP, and 1× protease inhibitor cocktail and solubilized with 1% (w/v) LMNG/PE (10 mol% PE in LMNG) for 1.5 h. Insoluble material was removed by centrifugation at 48,000 × *g* for 1 h. The clarified supernatant was incubated with Strep-Tactin resin pre-equilibrated in 1 mM SAM, 0.01% LMNG/PE in Buffer A for 2 h. The resin-bound protein was incubated with purified Fab8D3-2 and MBP-PrA/G for legobody assembly. Following assembly, the resin was washed with 2 mM maltose, and the complexes were eluted with 5 mM D-desthiobiotin in Buffer A containing SAM and PE as above. The eluates were concentrated using a 100-kDa molecular-weight cutoff concentrator and further purified by size-exclusion chromatography on a Superose 6 Increase 10/300 GL column. The running buffer contained 0.001% LMNG/PE and 0.2 mM SAM, 2 mM maltose, 0.2 mM TCEP, 150 mM NaCl, and 20 mM Tris-HCl (pH 8.0). Peak fractions were pooled and concentrated to 7.5 mg mL^{-1}. Immediately before cryo-EM grid preparation, SAM was added to a final concentration of 1 mM. Protein concentrations were determined from absorbance

at 493 nm using a theoretical extinction coefficient of 64,220 M^{-1} cm^{-1}.

To capture hPEMT with both products (PC and SAH), the purification procedure was the same as for $hPEMT^{PE+SAM}$, except that 10 mol% of PC and 1 mM SAH were included in the buffer throughout the purification process. Protein was concentrated to 10 mg mL^{-1}.

Purification of PmtA

E. coli BL21(DE3) cells carrying the MBP-PmtA expression plasmid were inoculated into LB medium supplemented with kanamycin and cultured overnight at 37 °C with shaking. The overnight culture was diluted 1:100 into 1 L of fresh LB medium containing kanamycin and grown at 37 °C until the OD_{600} reached approximately 0.6. Protein expression was induced with 0.2 mM IPTG, and cells were cultured at 20 °C for an additional 18 h. Cell pellets were resuspended in 25 mL lysis buffer containing 150 mM NaCl, 50 mM NaH_2PO_4, pH 8.0, supplemented with 1 mM PMSF, 0.5 mg mL^{-1} DNase I, and 5 mM $MgCl_2$. Cells were lysed using a high-pressure homogenizer, and insoluble material was removed by centrifugation at 25,000 × *g* for 30 min. The clarified lysate was incubated with 3 mL Ni-NTA resin at 4 °C for 2 h with gentle mixing. The resin was transferred to a gravity-flow column, washed with 20 column volumes (CV) of lysis buffer supplemented with 30 mM imidazole, and the bound protein was eluted with 300 mM imidazole in lysis buffer. Protein concentration was determined by measuring the absorbance at 280 nm using a theoretical molar extinction coefficient of 83,310 M^{-1} cm^{-1}.

Cryo-EM sample preparation and data collection

Two microliter of sample was applied onto glow-discharged Quantifoil Au R1.2/1.3 (300 mesh) grids and blotted for 5 s with force of 0 against filter paper equilibrated with 100% humidity at 8 °C in a Vitrobot Mark IV (FEI) chamber. The grids were flash plunged into liquid ethane for cryo-cooling.

Cryo-EM data collection and processing

Grids for the nanodisc-reconstituted samples were loaded onto a Titan Krios G4 cryo-electron microscope (Thermo Fisher Scientific) equipped with a Falcon 4i direct electron device and a Selectris X energy filter. Grids for the detergent-solubilized samples were loaded onto a Titan Krios cryo-electron microscope (Thermo Fisher Scientific) equipped with a Gatan K3 direct electron detector. Movie stacks were collected automatically using the EPU software (version 3.8.1 Thermo Fisher) with the Falcon 4i detector operating in counting mode at a total dose of 50 $e^-/Å^2$. Data processing was performed using cryoSPARC (v4.7.1). Motion correction and contrast transfer function (CTF) estimation were carried out for all micrographs. Particles were picked using blob picking (box size 256 pixels, binned by 4), followed by 2D classification, *ab initio* model generation, and heterogeneous refinement. Particles were then re-extracted (box size 256 pixels) and subjected to multiple rounds of heterogeneous refinement. Particles for the nanodisc-reconstituted samples were recentered to the hPEMT part and reextracted with a box size of 320 pixels. Final particle stacks were subjected to reference-based motion correction (particle polishing), followed by non-uniform refinement and local refinement. Map resolution was estimated using the gold-standard Fourier shell correlation (FSC) criterion of 0.143. Data processing strategies were summarized in **Fig. S2, S5, S7-S9**.

Model Building

Models were built manually using Coot 0.9.6[73] and refined using Phenix 1.19.2-4158[74]. Structures were visualized using PyMOL 2.3.3 and ChimeraX 1.11[75].

DATA AVAILABILITY

The coordinates for the models and the cryo-EM maps generated in this study have been deposited in the PDB and EMDB under the following accession codes:

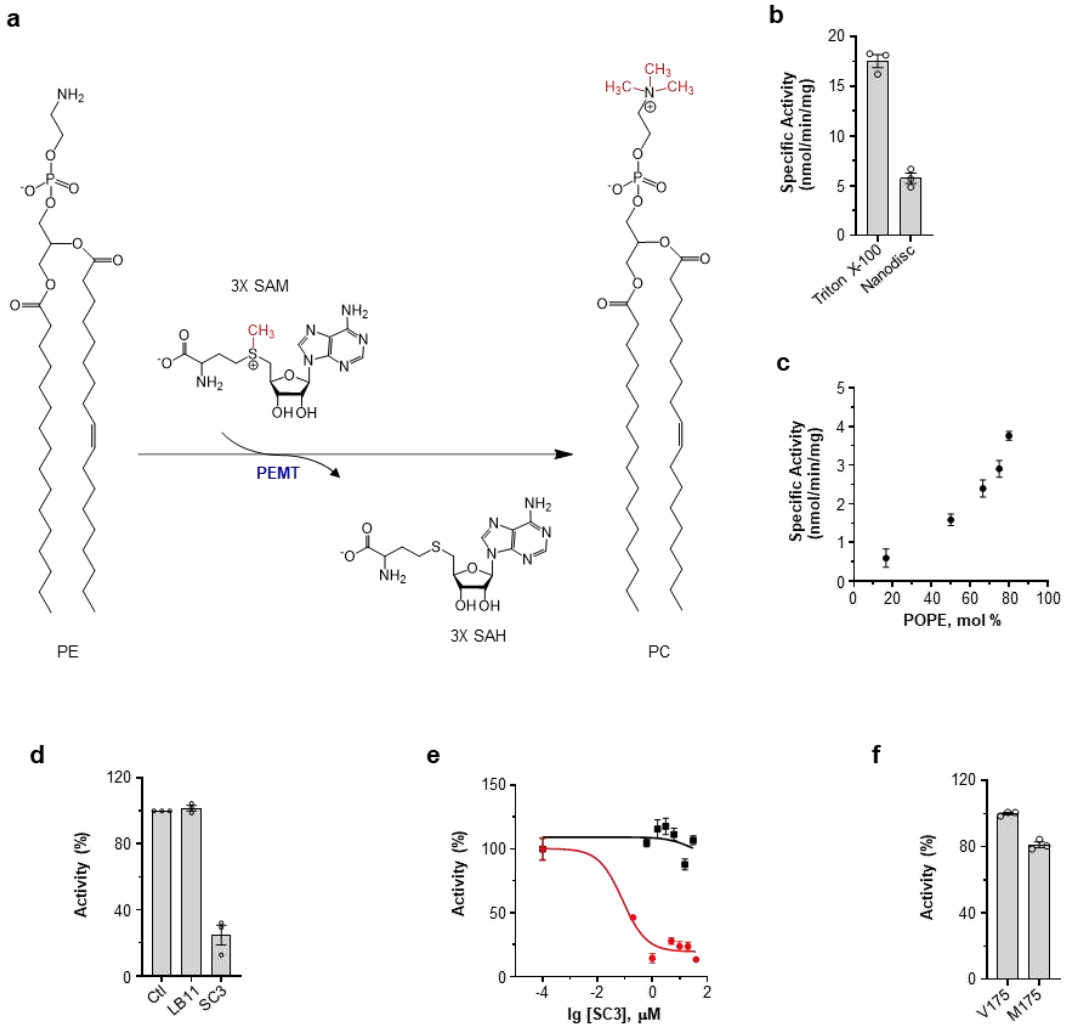
946 hPEMT^{PE+SAH}, 44UQ and EMD-82969; hPEMT^{PE+SAM}, 44UN and EMD-82968;
947 hPEMT^{PC+SAH}, 44UM and EMD-82967; hPEMT^{PE}, 44UI and EMD-82963;
948 hPEMT$^{CFA+SAH}$, 44UJ and EMD-82964.
949
950 **ACKNOWLEDGEMENT**
951 We thank the staff members of the Center of Cryo-EM at Sun Yat-sen University, of the
952 Core Facility of Shanghai Medical College at Fudan University, of the Core Facility of
953 Molecular Biology at the Center for Excellence in Molecular Cell Science, Chinese
954 Academy of Sciences, and of the Shenzhen Medical Academy of Research and
955 Translation (SMART). We thank Prof. Markus Seeger and Dr. Cedric A.J. Hutter at
956 University of Zurich, Switzerland for providing the sybody libraries and technical
957 guidance. This work has been supported by the National Natural Science Foundation
958 of China (32471246 & W2412096, DL; 32571459, T.L.; 82521001 to Q.Q.) and the
959 start-up funds from Sun Yat-sen University.
960
961 **AUTHOR CONTRIBUTION**
962 T.L. and H.X. purified protein and performed enzymatic assay with help from J.L.. T.L.
963 and Y.C. prepared grids, and collected cryo-EM data. T.L., Q.Q., and D.L. processed
964 cryo-EM data. D.L. conceptualize the project and wrote the manuscript with inputs
965 from T.L., H.X., Z.Y., and Q.Q..
966
967 **COMPETING INTEREST STATEMENT**
968 The authors declare no competing interests.

Supplementary Information

Supplementary Fig. 1-10

Still image and caption for Movie 1

Supplementary Table 1



977

978

979 **Fig. S1 | Functional characterization of hPEMT. a** Reaction catalyzed by hPEMT. **b**

980 Activity of hPEMT in Triton X-100 micelles and lipid nanodiscs. **c** Activity of hPEMT

981 as a function of PE concentration in Triton X-100 micelles. **d** Activity of hPEMT in the

982 presence of a control nanobody, LB11, or SC3 at 5 μM concentration. **e** Activity of

983 hPEMT under varying SC3 concentrations in Triton X-100 (black) and laurylmaltose

984 neopentylglycol (LMNG) (red) micelles. **f** Activity comparison of the V175 and M175

985 variants. Data in **c-f** represent mean ± s.e.m. from three independent experiments.

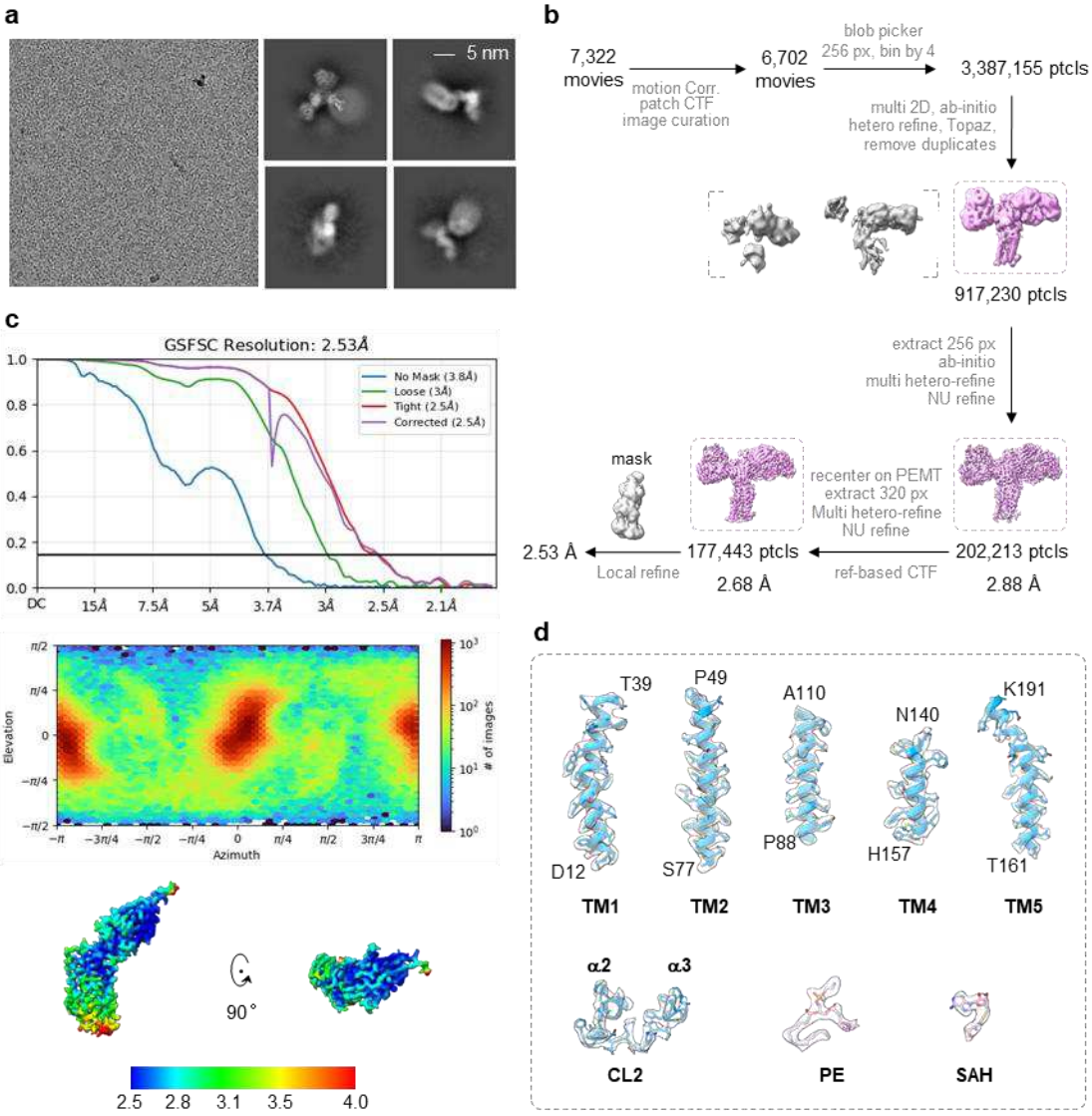


Fig. S2 | Cryo-EM data processing and representative density features of hPEMT^{PE+SAH}. a Representative cryo-EM micrograph and selected 2D class averages. **b** Cryo-EM data processing workflow. **c** Gold-standard FSC curve (top), angular distribution heat map (middle), and local resolution estimation (bottom). Density for the legobody part is omitted for clarity. **d** Representative cryo-EM densities.

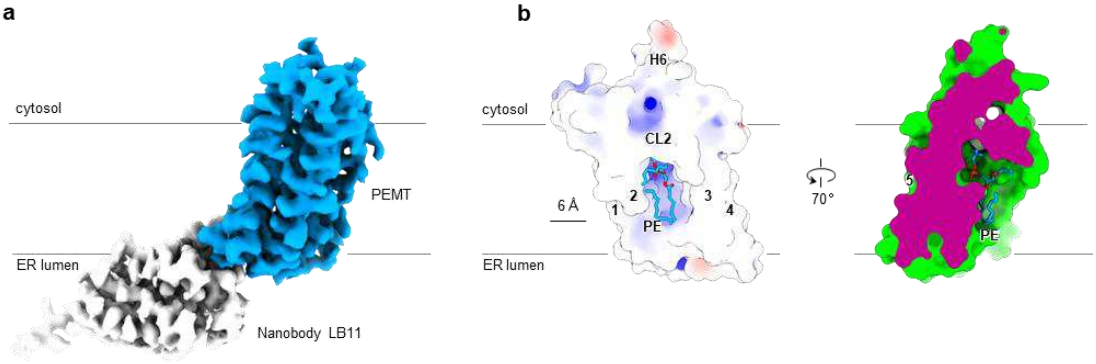


Fig. S3 | Structure of hPEMT reconstituted in lipid nanodiscs. a Cryo-EM map of hPEMT (blue) bound to LB11 (white). Legobody density is omitted for clarity. **b** Electrostatic surface (left) and molecular surface (right) views of hPEMT highlighting the PE-binding cavity. The surface is clipped to expose the binding pocket.



998

999

1000 **Fig. S4 | Sequence alignment of PEMT orthologs.** Sequence alignment of

1001 evolutionarily representative PEMT orthologs. Uniprot accession numbers and

1002 sequence identity/similarity relative to human PEMT are indicated (%). Asterisks,

1003 colons, and dots denote identical, conserved, and semi-conserved residues, respectively.

1004 TMH denotes transmembrane helices and α denotes non-transmembrane helices. TMH-

1005 capping proline residues are highlight in yellow. Asp120, a co-factor binding residue,

1006 is highlighted in green. TMH and their extensions are indicated above the alignment by

1007 filled and half-filled bars, respectively.

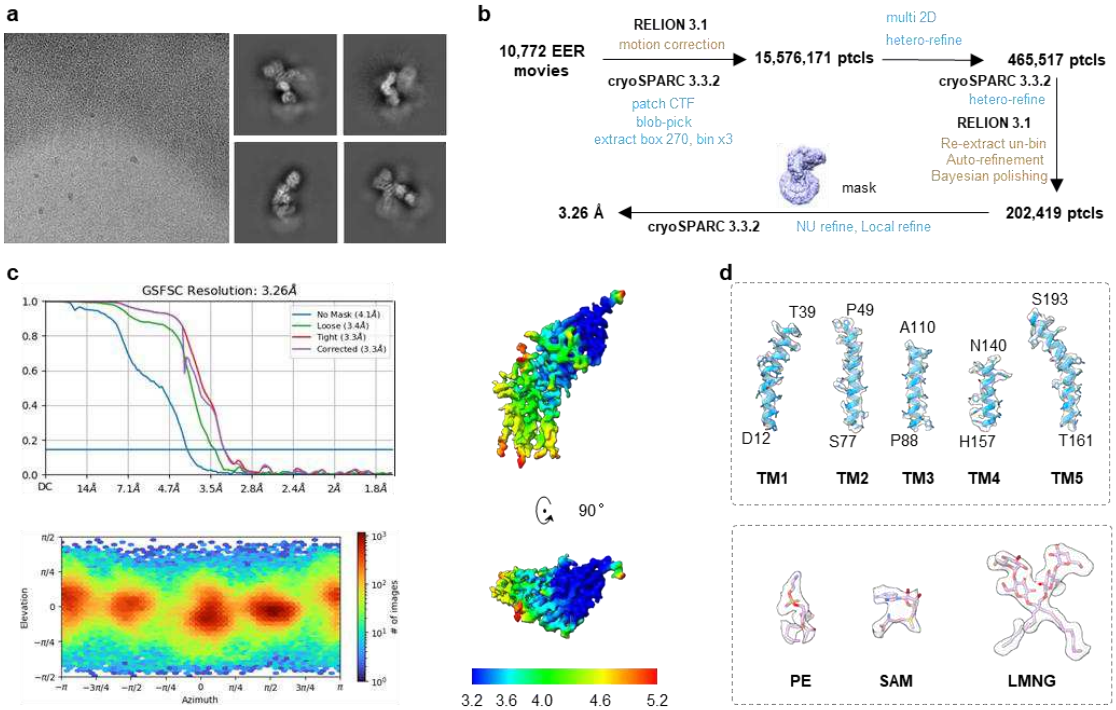


Fig. S5 | Cryo-EM data processing and representative density features of hPEMT^{PE+SAM}. a Representative cryo-EM micrograph and selected 2D class averages. **b** Cryo-EM data processing workflow. **c** Gold-standard FSC curve (top), angular distribution heat map (middle), and local resolution estimation (bottom). Density for the legobody part is omitted for clarity. **d** Representative cryo-EM densities.

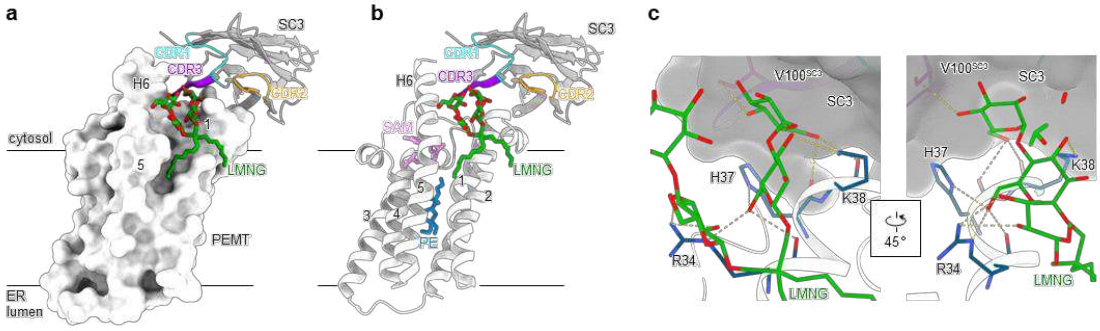


Fig. S6 | Interactions between SC3 and hPEMT. a,b Overall structure of the hPEMT-SC3 complex shown as surface (**a**) or cartoon (**b**). hPEMT is colored white and SC3 grey, with CDR1–3 colored as indicated. LMNG (green) and PE (cyan) are shown as sticks. **c** Detailed interactions among the CDR3 loop of SC3 (magenta and semi-transparent surface), hPEMT (white cartoon with blue surface), and LMNG (green). Dashed lines indicate interactions within 3.4 Å.

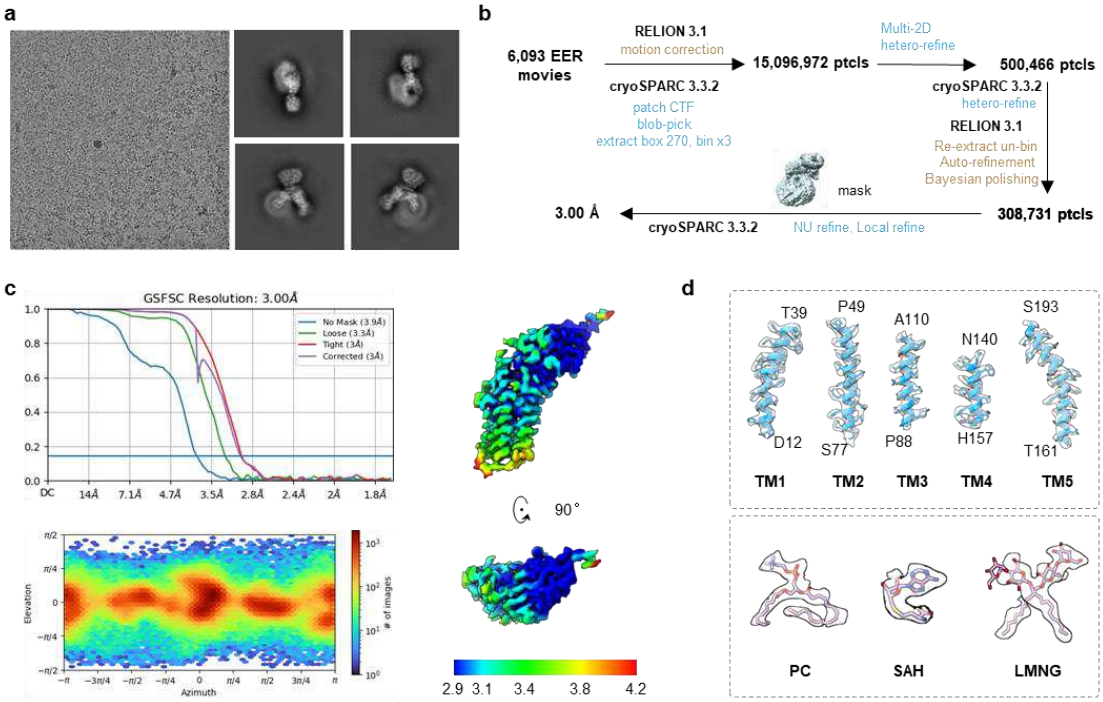


Fig. S7 | Cryo-EM data processing and representative density features of hPEMT^{PC+SAH}. a Representative cryo-EM micrograph and selected 2D class averages. **b** Cryo-EM data processing workflow. **c** Gold-standard FSC curve (top), angular distribution heat map (middle), and local resolution estimation (bottom). Density for the legobody part is omitted for clarity. **d** Representative cryo-EM densities.

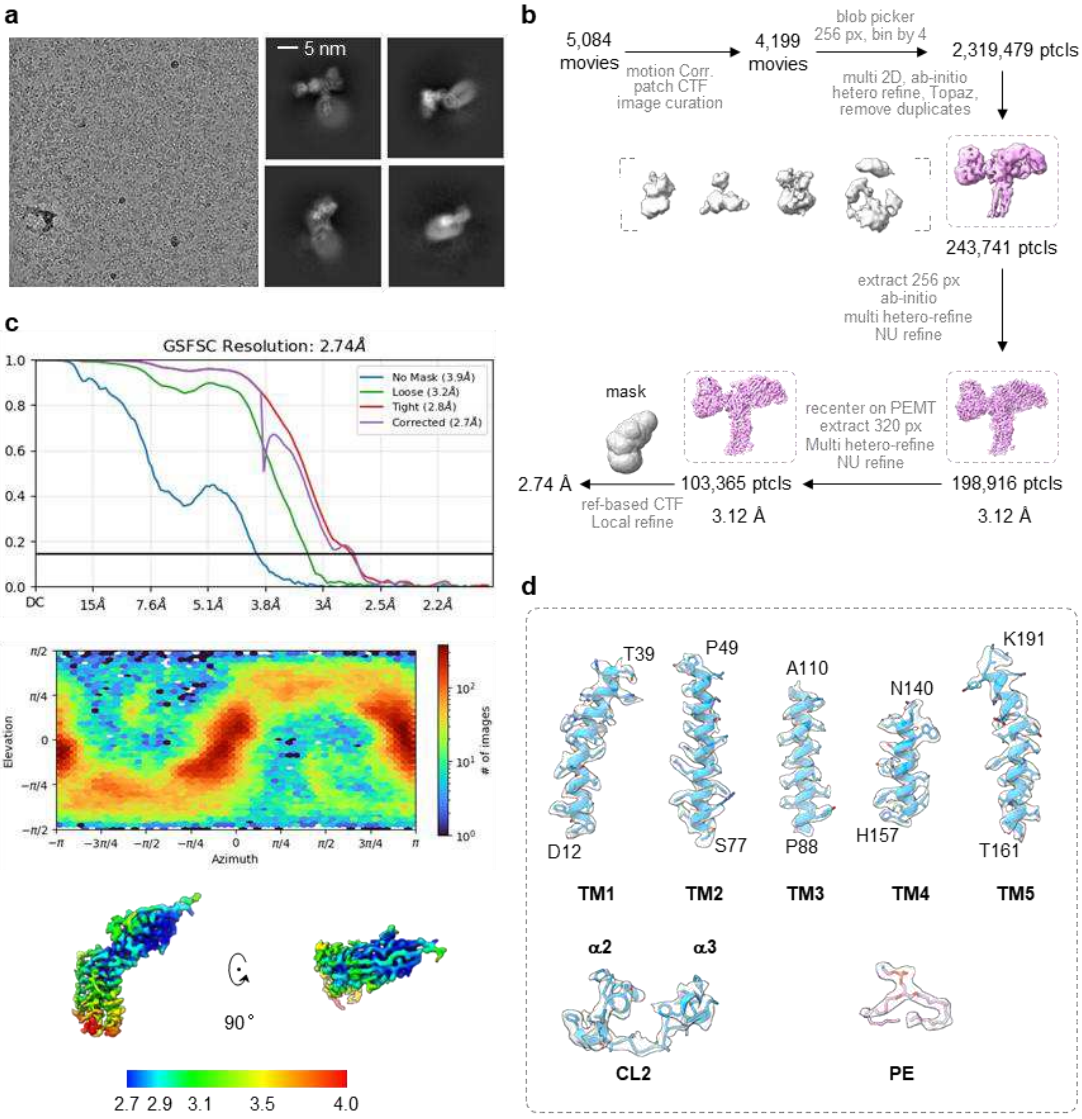


Fig. S8 | Cryo-EM data processing and representative density features of hPEMT^{PE}. a Representative cryo-EM micrograph and selected 2D class averages. **b** Cryo-EM data processing workflow. **c** Gold-standard FSC curve (top), angular distribution heat map (middle), and local resolution estimation (bottom). Density for the legobody part is omitted for clarity. **d** Representative cryo-EM densities.

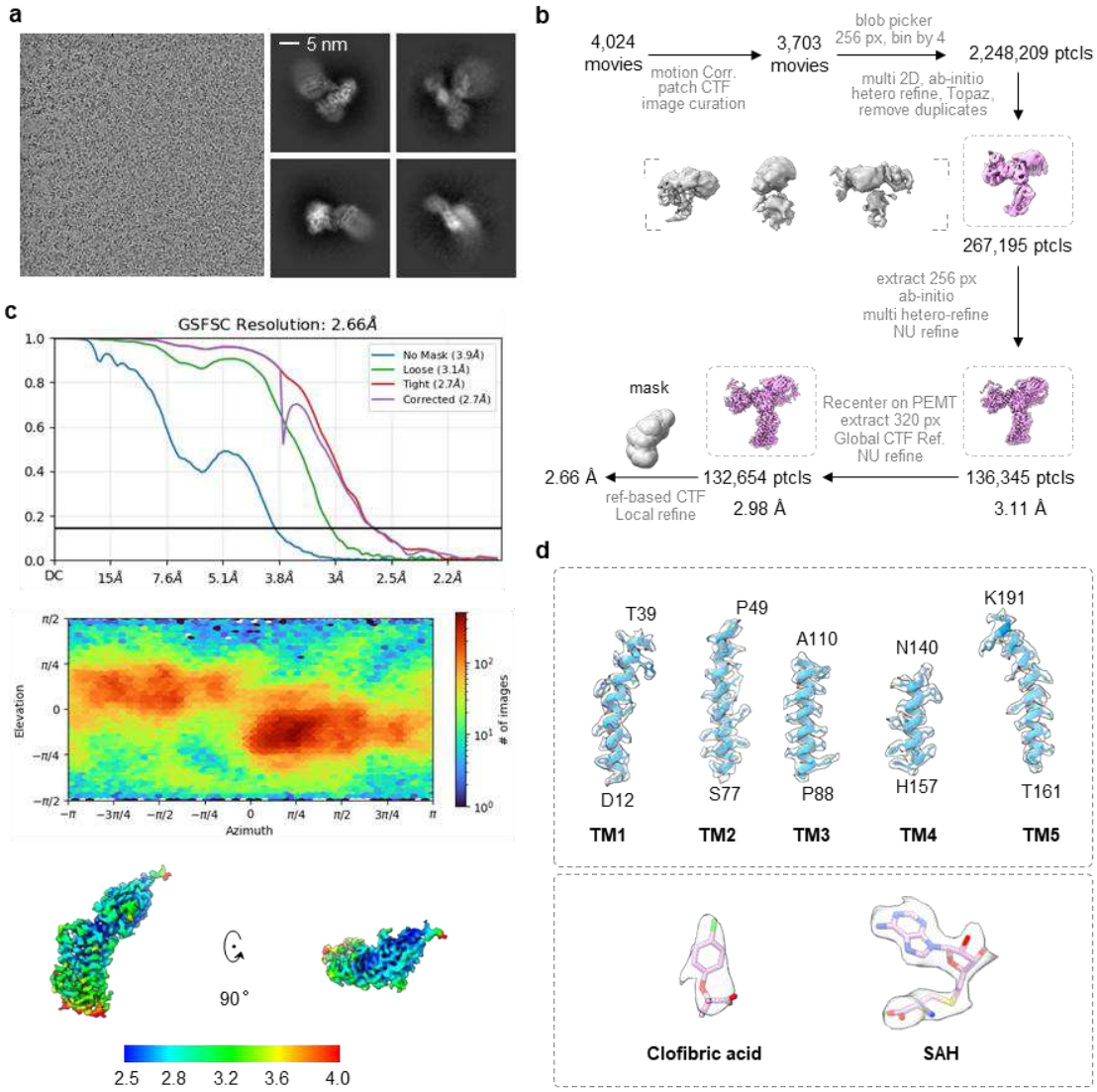


Fig. S9 | Cryo-EM data processing and representative density features of hPEMT-2m bound with CFA (hPEMT$^{CFA+SAH}$). a Representative cryo-EM micrograph and selected 2D class averages. **b** Cryo-EM data processing workflow. **c** Gold-standard FSC curve (top), angular distribution heat map (middle), and local resolution estimation (bottom). Density for the legobody part is omitted for clarity. **d** Representative cryo-EM densities.

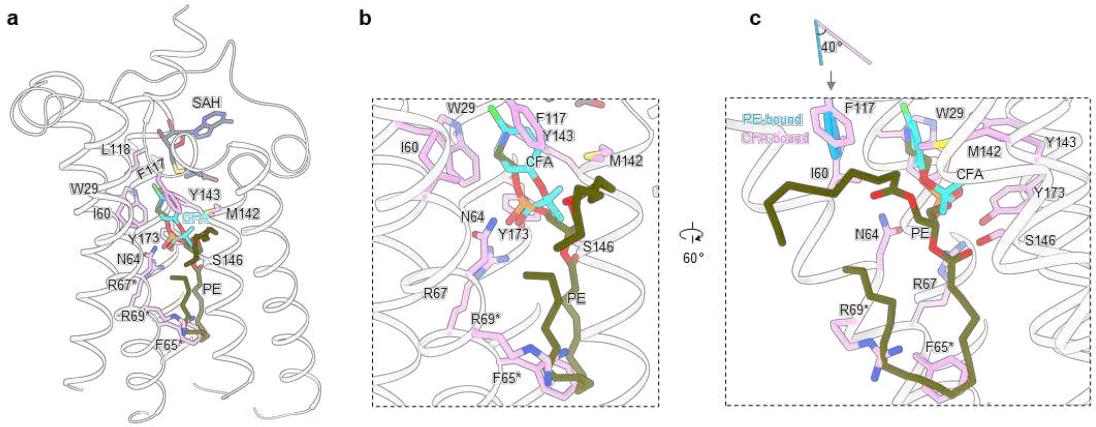
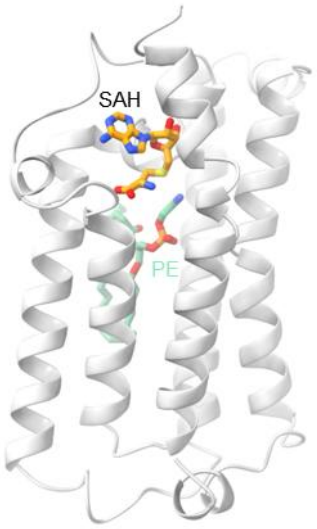


Fig. S10 | CFA occupies the PE-binding cavity. a Overall structure of CFA/SAH-bound hPEMT2m. PE from the hPEMT nanodisc structure is superimposed for comparison. **b, c** Enlarged views of the CFA- and PE-binding sites. hPEMT residues are shown as pink sticks. CFA (cyan) and PE (brown) are shown as thicks. Asterisks indicate the F65R and S68F substitutions.



Movie 1 | Conformational transition between the SAH-bound (hPEMT^{PE+SAH}) and SAH-free (hPEMT^{PE}) states. The molecular morph was generated using ChimeraX, with relevant structural elements labeled accordingly.

Table S1. Cryo-EM data collection and refinement statistics.

	hPEMT^{PE+SAH}	hPEMT^{PE+SAM}	hPEMT^{PC+SAH}	hPEMT^{PE}	hPEMT^{CFA}
Data collection					
Magnification	130 k	105 k	105 k	105 k	105 k
Voltage (kV)	300	300	300	300	300
Electron exposure ($e^-/Å^2$)	50	50	50	50	50
Defocus range (μm)	-2.2 to -1.2	-2.5 to -1.5	-2.5 to -1.5	-2.2 to -1.2	-2.2 to -1.2
Pixel size (Å)	0.934	0.832	0.832	0.949	0.949
Symmetry imposed	C1	C1	C1	C1	C1
Initial particle images (No.)	3,387,155	15,576,171	15,096,972	2,319,479	2,248,209
Final particle images (No.)	177,443	202,419	308,731	103,365	132,654
Map resolution (Å)	2.53	3.26	3.00	2.74	2.66
FSC threshold	0.143	0.143	0.143	0.143	0.143
Refinement					
Model resolution (Å)	2.9	3.4	3.3	3.2	3.0
FSC threshold	0.5	0.5	0.5	0.5	0.5
Map sharpening *B* factor ($Å^2$)	-72.1	-135.5	-130.0	-81.7	-82.0
Model composition					
Non-hydrogen atoms	2,576	4,821	8,775	2,512	2,587
Protein residues	321	615	1,181	321	321
Ligands / ion	2	3	4	1	2
B factor ($Å^2$)					
Protein	69.95	57.28	53.40	73.28	81.68
Ligand	81.35	71.14	45.40	80.80	99.66
R.m.s. deviations					
Bond lengths (Å)	0.005	0.011	0.003	0.004	0.005
Bond angles (°)	0.764	1.353	0.646	0.678	0.793
Validation					
MolProbity score	1.66	3.29	1.67	1.38	2.33
Clashscore	5.98	46.44	14.59	6.94	14.54
Ramachandran plot					
Favored (%)	98.74	97.52	98.19	98.11	96.85
Allowed (%)	1.26	2.48	1.81	1.89	3.15
Outliers (%)	0.00	0.00	0.00	0.00	0.00

Supplementary Files

This is a list of supplementary files associated with this preprint. Click to download.

- PEMT.mp4